

Analysis of Cloud-Resolving Model Simulations for Scale Dependence of Convective  
Momentum Transport

Yi-Chin Liu<sup>1,2</sup>, Jiwen Fan<sup>1,\*</sup>, Kuan-Man Xu<sup>3</sup>, Guang J. Zhang<sup>4</sup>

<sup>1</sup> Pacific Northwest National Laboratory, Richland, Washington, USA

<sup>2</sup> Air Resources Board, California Environmental Protection Agency, California, USA

<sup>3</sup> NASA Langley Research Center, Hampton, Virginia, USA

<sup>4</sup> Scripps Institution of Oceanography, University of California, San Diego, California, USA

\* Corresponding author:

Jiwen Fan, Senior Scientist, Pacific Northwest National Laboratory

509/375-2116 (o)

[Jiwen.fan@pnnl.gov](mailto:Jiwen.fan@pnnl.gov)

## Abstract

We use 3-D cloud-resolving model (CRM) simulations of two mesoscale convective systems at mid-latitudes and a simple statistical ensemble method to diagnose the scale dependency of convective momentum transport (CMT) and CMT-related properties, and evaluate a parameterization scheme for convection-induced pressure gradient (CIPG) developed by Gregory et al. (GKI97). GKI97 relates CIPG to a constant coefficient multiplied by mass flux and vertical mean wind shear. CRM results show that mass fluxes and CMT exhibit strong scale dependency in temporal evolution and vertical structure. The prevalent understandings of CMT characteristics in terms of upgradient/downgradient transport are applicable to updrafts but not downdrafts across a wide range of grid spacings (4-512 km). For the small-to-median grid spacings (4~64 km), GKI97 reproduces some aspects of CIPG scale dependency except for underestimating the variations of CIPG as grid spacing decreases. However, for large grid spacings (128~512 km), GKI97 might even less adequately parameterize CIPG because it omits the contribution from either the nonlinear shear or buoyancy forcings. Further diagnosis of CRM results suggests that inclusion of nonlinear shear forcing in GKI97 is needed for the large grid spacings, and use of the three-updraft and one downdraft approach proposed in an earlier study may help a modified GKI97 capture more variations of CIPG as grid spacing decreases for the small-to-median grid spacings. Further, the optimal coefficients used in GKI97 seems insensitive to grid spacings, but they might be different for updrafts and downdrafts, for different MCS types, and for zonal and meridional components.

## 1. Introduction

Convective momentum transport (CMT), which refers to transport of horizontal momentum in the vertical direction by cumulus clouds, occurs mostly in the troposphere and has been demonstrated to have an essential impact on global atmospheric circulations and climate in both observational and numerical studies (e.g., Houze 1973; LeMone 1983; Helfand 1979; Zhang and McFarlane 1995; Song et al. 2008; Richter and Rasch 2008; Majda and Stechmann, 2008, 2009, 2016; Khouider et al. 2012a, b; Shaw and Lane 2013; Land and Moncrieff 2010; Moncrieff and Liu 2006). However, it is a challenging task to fully understand CMT and parameterize it because (1) CMT cannot be directly measured on a global scale, and instead is estimated as a residual from the small imbalance between the large-scale horizontal pressure gradient force (PGF) and the Coriolis force from intensive field experiments (Sui and Yanai 1986; Wu and Yanai 1994; Tung and Yanai 2002a, b), (2) CMT is not a conserved variable and comprises two horizontal components that can behave differently for different mesoscale convective systems (MCSs) (Asai 1970; LeMone 1983; LeMone and Jorgensen 1991; Wu and Arakawa 2014), and (3) CMT has multiscale features ranging from cloud clusters on mesoscale to convectively coupled equatorial waves (CCW) on equatorial synoptic scales (Majda and Stechmann 2009; Khouider et al. 2012a, b).

Most observational data and theoretical studies suggest that CMT is often downgradient in non-linear MCSs, and can be either upgradient or downgradient for linear MCSs (Moncrieff and Green 1972; LeMone et al. 1984; Moncrieff 1992; Grabowski and Moncrieff 2001; Khouider et al. 2012b; Majda and Stechmann 2009). For non-linear MCSs, such as mesoscale convective complex (MCC), Sui and Yanai (1986) and Tollerud and Esbensen (1983) utilized data from Phase III of Global Atmospheric Research Program (GARP) Atlantic Tropical Experiment (GATE) and

discovered that non-linear MCSs tend to decelerate the large-scale flow in the upper troposphere as well as reduce the vertical wind shear in the lower troposphere. Therefore, CMT is downgradient with respect to mean wind shear. Wu and Yanai (1994) found that CMT is downgradient in the upper troposphere for MCC using observation data from the Oklahoma-Kansas Preliminary Regional Experiment for STORM-Central (OK PRE-STORM) and Atmospheric Variability Experiment-Severe Environmental Storms and Mesoscale Experiment (SESAME).

For linear MCSs, Asai (1970), LeMone (1983), Gallus and Johnson (1992), and Wu and Yanai (1994) have consistently shown that the line-parallel component of CMT is downgradient, but the line-normal component of CMT is upgradient. LeMone and Jorgensen (1991) reported that for cloud systems during the Taiwan Area Mesoscale Experiment, the line-normal component of CMT is downgradient in the lower troposphere but becomes upgradient in the upper troposphere. Zhang and Wu (2003) used 2-D cloud-resolving model (CRM) to study the CMT of tropical convection observed during the Tropical Ocean and Global Atmosphere Coupled Ocean-Atmosphere Response Experiment Intensive Observation Period, and they pointed out that the CMT in the easterly wind regime is downgradient, but CMT in the westerly wind burst is upgradient. Houze et al. (2000) uses Doppler radar data collected by aircraft and ship and found that CMT was downgradient within the westerly onset region and was upgradient within the westerly wind burst. Khouder et al. (2012b) employed a multicloud model and suggested that CMT associated with convectively coupled wave (CCW) in front of the Madden-Julian Oscillation (MJO) is downgradient, while the CMT associated the squall lines east of the convection core is upgradient.

Many studies have attempted to parameterize the effect of CMT in general circulation models (GCMs) (e.g., Schneider and Lindzen 1976, hereafter SL76; Zhang and McFarlane 1995;

93 Gregory et al. 1997, hereafter GKI97). Despite the complexity of CMT, this effect is often  
 94 formulated in a grossly simplified way. In the early years of CMT parameterization development,  
 95 CMT was parameterized in a simplified form by assuming that in-cloud horizontal momentum  
 96 depends only on lateral detrainment and entrainment rates (Ooyama 1971; SL76). However, since  
 97 LeMone (1983) and LeMone et al. (1984) demonstrated that in-cloud horizontal momentum can  
 98 also be strongly influenced by the convection-induced pressure gradient (CIPG) using  
 99 observational data from field experiments, many studies attempted to include the effects of CIPG  
 100 on in-cloud momentum in their CMT parameterization schemes (Zhang and Cho 1991a, b,  
 101 hereafter ZC91; Wu and Yanai 1994; GKI97). To include the CIPG effect in the CMT  
 102 parameterization, ZC91 parameterized CIPG in terms of cloud-scale circulation and the interaction  
 103 between convective updrafts/downdrafts and vertical mean wind shear. Wu and Yanai (1994) and  
 104 GKI97 represented the CIPG by assuming that it is proportional to the product of cloud mass flux  
 105 and vertical mean wind shear. Cheng and Xu (2014) parameterized the CIPG effect by using a  
 106 multiscale modeling framework (MMF), which is also known as superparameterization  
 107 (Khairoutdinov and Randall 2001). MMF consists of a 2-D CRM embedded in each grid column  
 108 of GCM, which can explicitly treat cloud-scale processes. The embedded CRM in the MMF  
 109 provides vertical transport of momentum in one horizontal direction, while in the other direction  
 110 the vertical momentum transport is assumed to be proportional to the vertical mass flux diagnosed  
 111 from the CRM in addition to the effects of entrainment and detrainment. In order to represent both  
 112 upgradient and downgradient vertical momentum transports, the orientation of the 2-D CRM varies  
 113 with time, which is determined by the stratification of the lower troposphere and environmental  
 114 wind shear. Tulich (2015) also developed a similar CMT parameterization scheme as Cheng and  
 115 Xu (2014) for the WRF model, which is referred to as the superparameterized version of the

Weather Research and Forecast model (SP-WRF). The SP-WRF can directly calculate the CIPG and CMT by using information obtained from a 2-D CRM with periodic lateral boundary.

Different from the aforementioned mixing-entrainment CMT parametrization schemes, Moncrieff (1981, 1992) parameterize the CMT effects by specifically considering the entire cumulus clouds and associated mesoscale circulation. They used analytical models to represent major flow patterns of squall lines, which allowed their parameterization scheme to capture the upgradient and downgradient features of CMT (LeMone and Moncrieff 1994). However, this analytical model requires several parameters such as the depth of the cloud and the detailed mesoscale flow pattern, which are not available in most of the general circulation models (GCMs). This limits the applicability of this scheme in conventional GCMs with parameterized physical processes.

One of the disadvantages of typical mixing-entrainment CMT parameterization schemes (i.e., SL76, GKI97, and ZC91) is requiring expensive computation resource. To provide cheaper alternatives, many studies have proposed different methods to parameterize CMT effects (Majda and Stechmann, 2008, 2009, 2016; Khouider et al. 2012a, b). Majda and Stechmann (2008, 2009) developed a simple stochastic model based on weak temperature gradient (WTG) approximation as well as a simple dynamic model, both of which are able to capture the important feature of CMT, including both upgradient and downgradient transport of CMT. Khouider et al. (2012a) developed an even simpler model to handle the upgradient and downgradient feature of CMT by using a similar approach to Majda and Stechmann (2008) but replaced the stochastic process with a simple exponential distribution function.

Using CMT parameterizations in GCMs has greatly improved the simulations and forecasting of large-scale circulations. For example, Helfand (1979) found an enhanced winter

Hadley circulation and more realistic simulated meridional winds when using a simple SL97 CMT scheme in the Goddard Laboratory for Atmospheric Sciences (GLAS) GCM model. Zhang and McFarlane (1995) obtained similar result to Helfand (1979) when including the ZC91 CMT parameterization in the Canadian Climate Centre model. Wu et al. (2003) successfully captured the seasonal migration of the Intertropical convergence zone (ITCZ) precipitation when the ZC91 CMT scheme was included in the National Center for Atmospheric Research Community Climate Model (CCM), version 3. Cheng and Xu (2014) showed that the stationary anomalous precipitation can be reduced and more realistic large scale circulation can be obtained when using their CMT parameterization scheme in the Community Atmosphere Model Version 3.5 (SPCAM). Tulich (2015) obtained improvement of tropical wave variability and the global simulations of seasonal climate when using his proposed CMT scheme in the WRF model. Hurricane intensity forecasting also showed promising improvement with the inclusion of the GKI97 CMT scheme in NCEP's operational Global Forecast System (GFS) and its nested Regional Spectral Model because the CMT scheme can effectively suppress spurious weak tropical disturbances (Han and Pan 2006). Deng and Wu (2010) also obtained a more coherent structure for the MJO deep convective center and its corresponding atmospheric variances when including a CMT scheme in the Iowa State University (ISU) GCM.

Richter and Rasch (2008) and Romps (2012) further compared two mixing-entrainment CMT schemes with and without CIPG. Both studies found that using the GKI97 scheme resulted in less improvement in the simulated large-scale circulations than using the SL76 scheme even though the GKI97 scheme was more physically representative than the SL76 scheme. One of the potential attributions of poorer performance of the GKI97 scheme is the high uncertainty in setting the coefficients in the formulation of CIPG in the GKI97 scheme. This uncertainty has been

reflected in the past studies in which different coefficients have been adopted, such as 0.7 by GKI97 and Richter and Rasch (2008), 0.55 by Zhang and Wu (2003), and 0.4 in CAM version 5.1 (CAM5.1) (Neale et al. 2010). In addition, the same coefficient has been used for both the zonal and meridional components of updraft- and downdraft-CIPG.

With increasing computing power, GCMs and regional climate models are able to run in a wide range of horizontal resolutions from hundreds of kilometers to a few kilometers. The aforementioned uncertainties may be amplified at higher spatial resolutions due to the lack of understanding of the scale dependency of CMT and CIPG. Improving this understanding is required to further improve CMT parameterizations, especially for the scale-adaptable aspects (Liu et al. 2015). Since the GKI97 scheme is one of the widely used CMT schemes in GCMs, it is important to reevaluate the performance of the GKI97 scheme and explore its adaptability to model resolution.

This study expands on the work of Zhang and Wu (2003), with the focus on diagnosing and exploring the scale dependency of CMT, CMT-related properties and evaluating the CIPG parameterization in the GKI97 scheme. Instead of using 2-D CRM simulations as in Zhang and Wu (2003), we utilize 3-D WRF model simulations with explicit spectral-bin microphysics (SBM) at the cloud-permitting scale for mid-latitude convective cloud systems (Fan et al. 2015). The scale-dependency of CMT and CMT related properties will be diagnosed using a simple statistical ensemble method that was proposed by Arakawa et al. (2011), Arakawa and Wu (2013), Wu and Arakawa (2014), and modified by Liu et al. (2015). The main goal of this study is twofold: 1) to explore the scale dependencies of mass flux, CMT, and CIPG for the mid-latitude convective cloud systems, and 2) to evaluate the formulation for parameterizing CIPG in the GKI97 scheme for different grid spacings.



## 2. Case description and CRM simulations

CMT can be different between MCCs and squall lines. To investigate the scale dependencies of CMT for both linear and nonlinear systems, one MCC case and one squall line case over the mid-latitude continent are selected for the CRM simulations. The two convection cases are from the Midlatitude Continental Convective Clouds Experiment (MC3E) near the DOE ARM Southern Great Plain (SGP) site (Petersen and Jensen 2012).

The simulations for the two cases are conducted using the Advanced Research WRF version 3.3.1 using the spectral-bin microphysics (SBM) (Khain et al. 2004; Fan et al. 2012) with open lateral boundaries. The SBM is an advanced microphysics scheme solving the microphysical processes explicitly based on the predicted particles over a number of size bins. It has more physical representations of microphysical processes compared with 1-moment and 2-moment bulk schemes, particularly in the hydrometeor diffusional growth and sub-cloud rain evaporation, as discussed in Wang et al. (2013). The detailed description of cases and the model simulations have been presented in Fan et al. (2015). Briefly, two cases have a horizontal domain size of  $560 \times 560$  km<sup>2</sup> with  $1 \times 1$  km<sup>2</sup> horizontal grid spacing and save model outputs every six minutes. The number of model vertical layers are 41 for MC3E-0523 and 45 for MC3E-0520. Liu et al. (2015) analyzed convective moisture transport. In this study, our analyses are also based on the same simulations. The analysis time period is 6 h for MC3E-0523 and 4 h for MC3E-0520.

## 3. Methodology

A simple statistical ensemble method presented by Arakawa et al. (2011), Arakawa and Wu (2013), and Wu and Arakawa (2014), and modified by Liu et al. (2015) is used to examine the scale-dependency of CMT and CMT related properties. The principle of this method is to divide

208 the CRM domain into subdomains with different horizontal sizes to mimic the GCM grid spacings  
 209 with the assumptions that different spatial locations are uncorrelated and have the same statistics.  
 210 First, we define clouds in convective updraft and downdraft regions using the following criteria  
 211 (Liu et al. 2015): (1) vertical velocities ( $w$ )  $> 1 \text{ m s}^{-1}$  and total hydrometeor mixing ratio ( $q_{tot}$ )  $>$   
 212  $1 \times 10^{-6} \text{ kg kg}^{-1}$  or (2)  $w > 2 \text{ m s}^{-1}$  for updrafts, and  $w < -1 \text{ m s}^{-1}$  and  $q_{tot} > 1 \times 10^{-5} \text{ kg kg}^{-1}$  for  
 213 downdrafts. Second, we divide the CRM domain,  $560 \text{ km} \times 560 \text{ km}$ , into subdomains with  
 214 horizontal sizes of  $2 \times 2$ ,  $4 \times 4$ ,  $8 \times 8$ ,  $16 \times 16$ ,  $32 \times 32$ ,  $64 \times 64$ ,  $128 \times 128$ ,  $256 \times 256$ , and  $512 \times 512 \text{ km}^2$   
 215 by excluding the outermost 24 km area on each side. A subdomain can belong to one of seven  
 216 different combinations of updraft, downdraft and environment. These subdomain types include (i)  
 217 updraft only, (ii) downdraft only, (iii) environment only, (iv) updraft and environment, (v)  
 218 downdraft and environment, (vi) updraft, downdraft, and environment, and (vii) updraft and  
 219 downdraft. Our analysis considers only types (iv), (v), and (vi) because as far as CMT  
 220 parameterization is concerned, types (i), (ii), and (iii) do not contribute to CMT. Although type  
 221 (vii) can have non-zero CMT due to differences in cloud properties between updrafts and  
 222 downdrafts, it only appears when the subdomain size is smaller than 16 km, and its contribution  
 223 to the total momentum transport (resolved momentum transport + CMT) is very small. Therefore,  
 224 we exclude type (vii) from the analysis as well.

225 The mathematical expressions for CRM-simulated CMT are provided below. Because  
 226 MC3E-0523 is a nonlinear MCC system, the two horizontal components are in the zonal ( $x$ ) and  
 227 meridional ( $y$ ) directions. For MC3E-0520 linear convective system (squall line), the two  
 228 horizontal components are converted to the line-parallel and the line-normal components. They  
 229 are also referred to as the  $x$ - and  $y$ -components, respectively. The CRM-simulated CMT in the  $x$

230  $(\overline{\rho w' u'})$  and y directions  $(\overline{\rho w' v'})$  from the CRM simulations are defined as (Wu and Arakawa 2014;  
 231 Zhang and Wu 2003):

$$232 \quad (\overline{\rho w' u'}) = \rho \frac{1}{N} \sum_{i=1}^N (w_i - \bar{w})(u_i - \bar{u}) \quad (1a)$$

$$233 \quad (\overline{\rho w' v'}) = \rho \frac{1}{N} \sum_{i=1}^N (w_i - \bar{w})(v_i - \bar{v}) \quad (1b)$$

234 where  $\rho$  is the air density.  $u_i$ ,  $v_i$ , and  $w_i$  are the  $x$ ,  $y$ , and vertical ( $z$ ) components of velocity ( $\text{m s}^{-1}$ )  
 235 at each CRM grid point  $i$  in a subdomain considered. Overbar and prime represent the mean over  
 236 the subdomain and the deviation from it, respectively.  $N$  is the total number of grid points in the  
 237 subdomain.  $\overline{\rho w' u'}$  and  $\overline{\rho w' v'}$  can be further partitioned into contributions from updrafts ( $U_{x_{crm}}$ ,  
 238  $U_{y_{crm}}$ ) and downdrafts ( $D_{x_{crm}}$ ,  $D_{y_{crm}}$ ) and environment ( $E_{x_{crm}}$ ,  $E_{y_{crm}}$ ), with similar definitions to  
 239 Eq. (1) except only those grid points satisfying their respective criteria are included, and the  
 240 summation is over  $N_U$ ,  $N_D$  and  $N_E$ , respectively. Here  $N_U$ ,  $N_D$  and  $N_E$  are the numbers of grid points  
 241 in a subdomain containing updrafts, downdrafts and environment, respectively. For a given grid-  
 242 spacing (e.g. 64 km), the number of such subdomains  $j$  within the CRM domain that meet  
 243 conditions of (iv), (v), and (vi) is denoted by  $M$ . Then the ensemble-mean  $x$ - ( $C_{x_{crm}}$ ) and  $y$ - ( $C_{y_{crm}}$ )  
 244 components of CMT of is given by

$$245 \quad C_{x_{crm}} = \frac{1}{M} \sum_{j=1}^M \rho (\overline{w' u'})_j \quad (2a)$$

$$246 \quad C_{y_{crm}} = \frac{1}{M} \sum_{j=1}^M \rho (\overline{w' v'})_j \quad (2a)$$

247 In terms of parameterizations of CMT, the traditional top-hat approach ignored  
 248 inhomogeneity within updrafts and downdrafts, and thus the subdomain-averaged updraft vertical  
 249 velocity and  $x$ - and  $y$ -component horizontal velocities are calculated by  $\hat{w}_U = \frac{1}{N_U} (\sum_{i=1}^{N_U} w_i)$ ,  $\hat{u}_U =$

250  $\frac{1}{N_U}(\sum_{i=1}^{N_U} u_i)$ , and  $\hat{v}_U = \frac{1}{N_U}(\sum_{i=1}^{N_U} v_i)$ , respectively. The parameterized  $x$  component of CMT  
 251 associated with updrafts, downdrafts and environment (referred to as  $Ux_{1draft}$ ,  $Dx_{1draft}$ , and  $Ex_{1draft}$ ,  
 252 respectively) in a subdomain using the one-draft (top-hat) approach is given by:

$$253 \quad Ux_{1draft} = \sigma_U(\hat{w}_U - \bar{w})(\hat{u}_U - \bar{u}) \quad (3a)$$

$$254 \quad Dx_{1draft} = \sigma_D(\hat{w}_D - \bar{w})(\hat{u}_D - \bar{u}) \quad (3b)$$

$$255 \quad Ex_{1draft} = \sigma_E(\hat{w}_E - \bar{w})(\hat{u}_E - \bar{u}) \quad (3c)$$

256 where subscripts  $U$ ,  $D$ , and  $E$  denote the updraft, downdraft and environment, respectively.  $\sigma_U$ ,  $\sigma_D$ ,  
 257 and  $\sigma_E$  are the fractions of updraft, downdraft and environmental areas, respectively. The  
 258 parameterized  $y$  component of updraft CMT ( $Uy_{1draft}$ ), downdraft CMT ( $Dy_{1draft}$ ), and environment  
 259 CMT ( $Ey_{1draft}$ ) in a subdomain with the one-draft approach can be obtained with similar definitions  
 260 to Eq. (3a)-Eq. (3c) except that  $u$ 's are replaced by  $v$ 's.

261 To account for the inhomogeneous structures of updrafts to better represent the convective  
 262 transport of water vapor, Liu et al. (2015) adopted a three-updraft approach. By applying the three-  
 263 updraft approach to the CMT,  $x$ - and  $y$ -components of updraft CMT (referred to as  $Ux_{3draft}$ ,  $Uy_{3draft}$ )  
 264 in a subdomain can be calculated by:

$$265 \quad Ux_{3draft} = \sigma_{U1}(\hat{w}_{U1} - \bar{w})(\hat{u}_{U1} - \bar{u}) + \sigma_{U2}(\hat{w}_{U2} - \bar{w})(\hat{u}_{U2} - \bar{u}) + \sigma_{U3}(\hat{w}_{U3} - \bar{w})(\hat{u}_{U3} - \bar{u}) \quad (4a)$$

$$267 \quad Uy_{3draft} = \sigma_{U1}(\hat{w}_{U1} - \bar{w})(\hat{v}_{U1} - \bar{v}) + \sigma_{U2}(\hat{w}_{U2} - \bar{w})(\hat{v}_{U2} - \bar{v}) + \sigma_{U3}(\hat{w}_{U3} - \bar{w})(\hat{v}_{U3} - \bar{v}) \quad (4b)$$

269

The three updrafts are defined as follows: 1)  $1 \text{ m s}^{-1} < w \leq 3 \text{ m s}^{-1}$ , and  $Q_{tot} > 10^{-6} \text{ kg kg}^{-1}$ , or  $2 \text{ m s}^{-1} < w \leq 3 \text{ m s}^{-1}$  for weak updrafts; 2)  $3 \text{ m s}^{-1} < w \leq 6 \text{ m s}^{-1}$  for medium-strength updrafts; and 3)  $w > 6 \text{ m s}^{-1}$  for strong updrafts (Arakawa and Wu 2013; Liu et al. 2015).

The vertical divergence of CMT is often called apparent momentum source ( $X$ ):

$$Xx = -\frac{\partial(\rho \overline{wru})}{\bar{\rho} \partial z} \quad (5a)$$

$$Xy = -\frac{\partial(\rho \overline{wrv})}{\bar{\rho} \partial z} \quad (5b)$$

The apparent momentum source for updrafts can be approximated by (Shapiro and Stevens, 1980; Wu and Yanai, 1994; Zhang and Wu, 2003):

$$Xx_U = M_U \frac{\partial \bar{u}}{\rho \partial z} + \delta(\hat{u}_U - \bar{u}) + \frac{1}{\rho} \sigma_U \left( \frac{\partial p}{\partial x} \right)_U \quad (6a)$$

$$Xy_U = M_U \frac{\partial \bar{v}}{\rho \partial z} + \delta(\hat{v}_U - \bar{v}) + \frac{1}{\rho} \sigma_U \left( \frac{\partial p}{\partial y} \right)_U \quad (6b)$$

where  $\delta$  is the air mass detrainment at the cloud boundaries, and  $p$  is the perturbation pressure induced by convection. The apparent momentum source for downdrafts ( $Xx_D$ ,  $Xy_D$ ) can be obtained with similar definitions to Eq. (6a)-Eq. (6b) except that subscript  $U$ 's are replaced by  $D$ 's. The first term on the right-hand side of (6a) and (6b) is the product of the updraft mass flux and the vertical mean wind shear, which can be interpreted as the vertical advection of mean horizontal momentum by compensating subsidence; the second term represents the effect of horizontal momentum that is detrained from updrafts into environment; the last term is the effect of the CIPG force on environment.

To further explore the scale dependency of CIPG, we adopt the approximated budget equation for CIPG from Zhang and Wu (2003):

$$\begin{aligned}
290 \quad \nabla^2(\nabla p) = & \nabla \left\{ -2\rho \left[ \frac{\partial w}{\partial x} \frac{\partial \bar{u}}{\partial z} + \frac{\partial w}{\partial y} \frac{\partial \bar{v}}{\partial z} \right] \right\} + \nabla \left\{ -2\rho \left[ \frac{\partial w}{\partial x} \frac{\partial u'}{\partial z} + \frac{\partial w}{\partial y} \frac{\partial v'}{\partial z} \right] \right\} + \nabla \left\{ -\rho \left[ \left( \frac{\partial u}{\partial x} \right)^2 + \right. \right. \\
291 \quad & \left. \left( \frac{\partial v}{\partial y} \right)^2 + \left( \frac{\partial w}{\partial z} \right)^2 \right] \right\} + \nabla \left\{ w^2 \rho \frac{\partial}{\partial z} \left( \frac{1}{\rho} \frac{\partial \rho}{\partial z} \right) \right\} + \nabla \left( \frac{\partial \rho B}{\partial z} \right) \quad (7)
\end{aligned}$$

292 Here,  $\nabla^2$  is the 3D Laplacian operator  $(\frac{\partial^2}{\partial x^2} + \frac{\partial^2}{\partial y^2} + \frac{\partial^2}{\partial z^2})$ . The first four terms on the right-hand  
 293 side represent the dynamic contributions to the Laplacian of CIPG, and are referred to as the linear-  
 294 shear forcing, nonlinear-shear forcing, the divergence forcing, and density stratification forcing,  
 295 respectively (Rotunno and Klemp 1982; Zhang and Wu 2003). The last term on the right-hand side  
 296 is the buoyancy forcing of the cloud air. To examine their relative contributions to the Laplacian  
 297 of CIPG, the first four terms on the right-hand side and the Laplacian of CIPG on the left-hand  
 298 side are directly calculated from CRM data, while the buoyancy term on the right-hand side is  
 299 estimated as the residual.

300 The GKI97 scheme includes only the linear-shear forcing for parameterizing CIPG and  
 301 can be expressed as:

$$302 \quad \frac{\sigma_U}{\rho} \left( \frac{\partial p}{\partial x} \right)_U = -c_{Ux} M_U \frac{\partial \bar{u}}{\partial z} \quad (8a)$$

$$303 \quad \frac{\sigma_D}{\rho} \left( \frac{\partial p}{\partial x} \right)_D = -c_{Dx} M_D \frac{\partial \bar{u}}{\partial z} \quad (8b)$$

$$304 \quad \frac{\sigma_U}{\rho} \left( \frac{\partial p}{\partial y} \right)_U = -c_{Uy} M_U \frac{\partial \bar{v}}{\partial z} \quad (8c)$$

$$305 \quad \frac{\sigma_D}{\rho} \left( \frac{\partial p}{\partial y} \right)_D = -c_{Dy} M_D \frac{\partial \bar{v}}{\partial z} \quad (8d)$$

306 where  $C_{Ux}$ ,  $C_{Dx}$ ,  $C_{Uy}$ , and  $C_{Dy}$  are coefficients. In the current GKI97 CMT scheme,  $C_{Ux}$ ,  $C_{Dx}$ ,  $C_{Uy}$ ,  
 307 and  $C_{Dy}$  are set to the same value (C). In the next section, we examine the relative contributions  
 308 from each forcing to the Laplacian of CIPG at different model grid spacings. This can provide  
 309 evidence for justifying the approximation used in the GKI97 scheme for all grid spacings.

To further quantify the performance of the GKI97 scheme for parameterizing CIPG at different grid spacings, we conduct a linear regression analysis for Eq. (8a)-Eq. (8d) using the product of mass flux and vertical mean wind shear as the predictor variable and CRM-derived CIPG as the response variable. The adjusted coefficient of determination ( $R_{adj}^2$ ) obtained from linear regression analysis indicates how well the CRM-derived CIPG variation can be explained by the product of mass flux and vertical mean wind shear (the GKI97 scheme). The formula for  $R_{adj}^2$  is as follows:

$$R_{adj}^2 = 1 - \left( \frac{SS_{resid}}{SS_{total}} \right) \times \left( \frac{n-1}{n-d-1} \right) = 1 - R^2 \left( \frac{n-1}{n-d-1} \right) \quad (9)$$

where  $R^2$  is the coefficient of determination, which is the ratio of  $SS_{resid}$  (the sum of the squared residuals from the regression) and  $SS_{total}$  (the sum of the squared differences from the mean of the dependent variable, or the total sum of squares),  $d$  is the total number of predictor variables in the regression equation, and  $n$  is the sample size. The larger  $R_{adj}^2$  is, the more variability in the response variable is explained by the predictor variables. In addition to  $R_{adj}^2$ , the Pearson correlation coefficient (CC) is also calculated to examine the linear dependence between the CRM-derived CIPG and the product of mass flux and vertical mean wind shear (Eq. 8).

The statistical significance for the regression analysis and CC is examined using the F-test and are considered statistically significant when satisfying the threshold to reject the null-hypothesis at 95% level. The statistical significance test can help discard unrealistic results that are obtained when the sample size is too small, especially when the grid spacing is large (128 km - 512 km).

Because the cloud mass flux is an important parameter for parameterizing the CMT in the GKI97 scheme, convective updraft and downdraft mass fluxes are also computed to explore their scale dependency. The updraft mass flux and downdraft mass flux are computed by:

$$M_U = \rho \sigma_U (\hat{w}_U - \hat{w}_E) \quad (10a)$$

$$M_D = \rho \sigma_D (\hat{w}_D - \hat{w}_E) \quad (10b)$$

Note that mean vertical velocity of environmental air  $\hat{w}_E$ , instead of grid-mean  $\bar{w}$ , is included.

## 4. Results

### 4.1 Scale dependency of CRM-simulated mass flux and CMT

Figure 1 shows the time-height cross sections of the ensemble mean grid-mean winds ( $\bar{u}$  and  $\bar{v}$ ) for 8 km and 128 km grid spacings from the MC3E-0523 case [see Fig. S1 in the supporting information (SI) for all different grid spacings]; hereafter, “ensemble mean” [see Eq. (2) for its definition] will be omitted for brevity. The analysis time period is from 1930 UTC 23 May to 0130 UTC 24 May, when the MCC evolves from the initial developing, intensifying, to mature stages. It shows that the grid-mean  $x$  component of winds ( $\bar{u}$ ) are westerly throughout the troposphere with the maximum wind speeds in the upper troposphere during the entire period (Figure 1a). The grid-mean  $y$  component of winds ( $\bar{v}$ ) are southerly in most of the troposphere except for 2100-2300 UTC above 10 km height and the maximum  $\bar{v}$  occurs in the lower troposphere (Figure 1b). In general, the time-height cross sections of  $\bar{u}$  and  $\bar{v}$  are very similar for different grid spacings, except weaker westerly winds and stronger northerly winds above 10 km altitude for larger grid spacings. This indicates a weak scale dependency for grid-mean wind components. The grid-mean  $x$  component of winds ( $\bar{u}$ ) from MC3E-0520 shows results similar to MCE-0523 (Figure 2a), demonstrating a weak scale dependency as well. However, the grid-mean



y component of winds ( $\bar{v}$ ) from MC3E-0520 exhibits distinct differences between small and large grid spacings (Figures. 2b and S2), as indicated by the gradual decrease of vertical gradient as the grid spacing increases from  $dx = 4\sim 16$  km to  $dx = 32\sim 512$  km.

To understand what contributes to the different vertical structures of  $\bar{v}$  between the small ( $dx = 4\sim 16$  km) and large ( $dx = 32\sim 512$  km) grid spacings from MC3E-0520, snapshots of the horizontal distribution of  $\bar{v}$  at 6.0 km altitude for  $dx = 8$  km and 128 km are shown in Figure 3. In Figures 3a-3b, only the subdomains that meet conditions (iv), (v), and (vi) for  $dx = 8$  km and 128 km are plotted to represent the small and large grid spacings, respectively. The selected subdomains for  $dx = 128$  km occupy much larger regions than those for  $dx = 8$  km. The latter are closer to where the squall line is located (Figure 3c). In addition, for  $dx = 128$  km the majority of the subdomains contain negative  $\bar{v}$ , resulting in negative ensemble-mean  $\bar{v}$ . However, for  $dx = 8$  km, the majority of the subdomains have positive  $\bar{v}$ , producing positive ensemble-mean  $\bar{v}$ . This explains the different upper level winds between large and small grid spacings, and how the scale dependency of  $\bar{v}$  comes from.

The updraft and downdraft mass fluxes show considerable differences among different grid spacings of MC3E-0523 (Figures 4 and S3 in SI). The updraft mass fluxes decrease monotonically as subdomain size/grid spacing ( $dx$ ) increases and peak from the initial developing stage at small grid spacings to the mature stage at very large grid spacings, while downdraft mass fluxes peak at  $dx = 8$  or 16 km and then decrease as  $dx$  increases (Figure S3). Note that subdomain size and grid-spacing are used interchangeably throughout the rest of the paper. In addition, downdraft mass fluxes peak near 4 km altitude where the freezing level is located and at the mature stage for all the grid spacings (Zhang and Wu 2003). The different temporal evolution between updraft mass fluxes and downdraft mass fluxes is because strong downdrafts do not develop coincidentally with

updrafts, and thus downdraft intensity is weaker at the early stage of development, and becomes stronger at the mature stage as strong precipitation forms. MC3E-0520 squall line shows similar results to MCE-0523 (Figures not shown), indicating that both updraft and downdraft mass fluxes have strong scale dependency.

As expected, the time-height cross sections of CMT show even larger differences among different grid spacings relative to those of either updraft or downdraft mass fluxes because CMT is the product of fluctuations of both horizontal and vertical wind components (Figs. 5 and S4). Here we only show results from MC3E-0523 as an example. Figure S4 shows that for all grid spacings the  $x$  component of updraft CMT is negative throughout the troposphere during 1930 UTC 23 May-0130 UTC 24 May. This indicates that there is downward momentum transport in westerlies. For small grid spacings, the updraft CMT peaks from the initial developing stage compared to the mature stage for the very coarse grid spacings, which is largely similar to updraft mass flux. For example, at  $dx = 4$  km (Figure S4a), the absolute maximum CMT occurs in the first few hours of development and then decreases significantly with time. At  $dx > 64$  km, the CMT magnitude is small at the first 2 hours of development and increases afterwards as in updraft mass flux (Figure 4a). Also, as the grid-spacing gets coarser, the CMT magnitude increases in the upper troposphere ( $> 10$  km altitude) perhaps due to better organized flows, for example, the anvil outflows.

Opposite to its  $x$ -component counterpart, the  $y$ -component of updraft CMT is mostly positive except for  $dx < 32$  km at the first hour and for  $dx > 32$  km below the 2 km altitude (Figures 6a and S5a), indicating mostly upward momentum transport in southerlies. Further, the magnitude increases with the grid spacing more significantly than that of its  $x$ -component counterpart.

Both  $x$ - and  $y$ -components of downdraft CMT show more significant changes as the grid spacing increases than their updraft counterparts (Figures. 5b, 6b, S4b, and S5b). For the  $x$  component of downdraft CMT (Figures 5b and S4b), as the grid spacing increases, it evolves from mostly negative at  $dx < 16$  km, to mostly positive at and above  $dx > 64$  km. As for the  $y$  component (Figures 6b and S5b), it evolves from mostly positive (except at low levels after 0000 UTC 24 May) for  $dx = 4$ -32 km to changing signs in the vertical for  $dx = 64$ -512 km, i.e., negative CMT at the 4-8 km altitude but positive CMTs below 4 km and above 8 km altitudes. As in the mass fluxes (Figure 4), downdraft CMTs peak in the lower troposphere while updraft CMTs are significant over a much larger extent of the troposphere.

In summary, the grid-unresolved properties, such as mass flux and CMT, have a much stronger scale dependency than grid-resolved properties, such as the grid-mean winds. Both CMT and mass fluxes have strong scale dependencies with CMT more stronger, but its temporal and vertical changes can be mostly explained by those of their corresponding mass fluxes. The magnitudes of updraft CMT depend on the organized flows that are stronger for the mature stage than for the initial stage of convective systems.

#### **4.2 Relationships between CMT and wind shear**

Previous studies have shown that for linear MCS such as squall line, CMT may be upgradient in the line-normal ( $y$ ) direction and downgradient in the line-parallel ( $x$ ) direction. On the other hand, CMT is generally downgradient for nonlinear MCS (Asai 1970; LeMone 1983; LeMone and Jorgensen 1991). To investigate whether the simulation reproduces the prevalent CMT characteristics and how the simulated CMT characteristics vary with grid spacings, the CMT profiles (updraft, downdraft and total) overlaid with the grid-mean vertical wind shear profile are shown in Figure 7. The grid-mean vertical  $x$ -component wind shear is calculated by:

$$(\bar{u}_{k+1} - \bar{u}_k)/|Z_{k+1} - Z_k| \quad (11)$$

where  $Z_k$  is the altitude of vertical level  $k$ . Because of the small differences in the results (discussed below) within either the large grid spacings or the small grid spacings group, we select results at  $dx = 128$  km and 8 km to represent the GCM scale and gray-zone scale, respectively, for brevity.

For MC3E-0523 (nonlinear MCS), comparing the  $x$ - and  $y$ -components of updraft and total CMTs with the grid-mean vertical wind shear shows that updraft and total CMT and vertical wind shear are generally opposite in sign at both large and small grid spacings, indicating that both the  $x$ - and  $y$ -components of total and updraft CMTs are downgradient with respect to vertical wind shear (Figure 7a). An exception occurs around the 7 km altitude for the  $y$ -component of  $dx = 128$  km. A similar downgradient transport can also be seen from the  $x$ - and  $y$ -components of downdraft CMT at  $dx = 8$  km but it is upgradient at  $dx = 128$  km. This suggests that downdraft CMT is very sensitive to grid spacing and can have different transport directions for small and large grid spacings, which is consistent with what is shown in Figures 5b and 6b, even though the downdraft CMT is much smaller than its updraft counterpart, especially in the upper troposphere.

For MC3E-0520 (linear MCS), the  $x$ -components of updraft, downdraft and total CMTs for  $dx = 8$  km and 128 km are generally opposite in sign to the grid-mean wind shear (except for downdraft CMT above the 8 km altitude at  $dx = 128$  km with small magnitudes), indicating downgradient transport (Figure 7b). As for the  $y$ -component, the relationship between CMTs and grid-mean wind shear exhibits some differences between  $dx = 8$  km and  $dx = 128$  km. At  $dx = 128$  km, the grid-mean wind shear above 2 km heights as well as updraft and total CMTs at all levels are positive, indicating an upgradient momentum transport while the downdraft momentum transport is downgradient at all levels (also for  $dx = 8$  km). At  $dx = 8$  km, the updraft and total CMTs are mostly positive at all levels, while the grid-mean vertical wind shears are negative above

7 km and below 2 km height, and are positive between 2 and 7 km height, which suggests an upgradient transport below 7 km height and downgradient transport above 7 km. The difference in the grid-mean wind shear can be deducted from the vertical profiles of grid-mean wind shear in the  $y$ -direction between  $dx = 8$  km and  $dx = 128$  km (Figure 2).

Based on the results shown above, for the nonlinear MCS (MC3E-0523), the downgradient transports for updrafts and total CMTs generally do not change with grid spacings and are consistent with previous studies. In contrast, downdraft CMT has downgradient transport at small grid spacings but becomes upgradient at large grid spacings. The upgradient CMT for downdrafts is consistent with Zhang and Wu (2003). As for the linear MCS (MC3E-0520), the downgradient transport in the line-parallel direction and upgradient transport in the line-normal direction suggested by previous studies are reproduced for updraft and total CMTs at both the small and large grid spacings except for the line-normal component above 7 km height at small grid spacings. The downdraft CMT, on the other hand, is always downgradient regardless of the grid spacings for both line-parallel and line-normal components. These results suggest that prevalent CMT characteristics based upon field campaigns and model calculation for spatial scales typical of current GCM resolution is applicable to updrafts but not downdrafts across a wide range of grid spacings examined in this study.

To explain why the characteristics of updraft CMT are different between the  $y$ - and  $x$ -components as well as between the small and large grid spacings for the  $y$ -component, snapshots of updraft CMT and updraft PGF in the line-parallel and line-normal directions are shown in Figures 8-11. These snapshots are similar to those shown in Figures 3a and 3b for the  $y$ -component winds. Figures 8 and 9 show the  $x$ -component of updraft CMT and PGF in convective updrafts at 4.5 km and 9 km altitudes, respectively, at 1500 UTC 20 May when the squall line is at the

intensifying stage. At 4.5 km altitude (Figure 8), the majority of the  $x$ -component of updraft CMTs is negative with exception for one subdomain at  $dx=128$  km and a few subdomains for  $dx = 8$  km. The negative  $x$  component of updraft CMT indicates that the air feeding the updrafts carries negative perturbation wind ( $u'$ ). Because the  $x$  component of updraft PGFs is mostly positive, the updraft PGF is opposite to the direction of the perturbation wind ( $u'$ ) in updrafts, decelerating the perturbation wind when air moves upward inside updrafts. As a result, the CMT at both large and small grid spacings is downgradient. A similar relation between the updraft CMT and PGF can also be seen at 9.0 km altitude except the updraft CMT is mainly positive while the updraft PGF is negative (Figure 9).

Figures 10-11 are the same as Figures 8-9, except for the line-normal component at 4.5 and 7.5 km altitudes. Note that 7.5 km instead of 9 km altitude is chosen because the  $y$ -component of maximum updraft CMT is located at a lower altitude. At 4.5 km altitude (Figure 10), the majority of line-normal updraft CMT at both small and large grid spacings is positive, indicating that the air entering convective updrafts carries positive perturbation wind ( $v'$ ). The positive  $y$ -component of updraft PGF is in the same direction as the perturbation wind ( $v'$ ) in the updrafts, accelerating the perturbation wind, resulting in upgradient CMT for both small and large grid spacings.

For large grid spacings at 7.5 km altitude, the  $y$ -component of updraft CMT and updraft PGF are mostly positive, indicating that the updraft PGF accelerates the perturbation wind in the updrafts, resulting in upgradient CMT. However, for small grid spacing, the majority of updraft CMT remains positive, but a large area of updraft PGF where the positive updraft CMT is located becomes negative, leading to decelerating the perturbation wind and downgradient CMT. This explains why the  $y$ -component of updraft CMT becomes downgradient transport above 7 km for small grid spacings. The results here suggest that the effect of PGF on updraft CMT characteristics

is consistent across all grid spacings. The aforementioned relationship between the updraft CMT direction and PGF has also been used to explain the different CMT characteristics in the westerly and easterly wind regimes in Zhang and Wu (2003).

To examine whether the CMT characteristics are also controlled by PGF in convective downdrafts, snapshots of downdraft CMT and PGF at 4.5 km altitudes in the  $x$ - and  $y$ -directions are also shown in Figures S6 and S7 in SI, respectively. Unlike the relation between the updraft CMT and PGF, the downdraft CMT and PGF do not have systematic relation for both the  $y$  and  $x$  components. The different signs of downdraft CMT when transitioning from the large to small grid spacings cannot be explained by the downdraft PGF as in updraft CMT. This may be expected because downdraft is largely contributed by precipitation, which could make the sign of downdraft CMT more influenced by the size of grid spacing via cloud microphysical processes.

#### **4.3. Scale dependency of apparent momentum source and CIPG**

Apparent momentum source is defined as the vertical gradient of CMT (Eq. 5). To examine the importance of CIPG to apparent momentum source, vertical profiles of the individual terms in Eq. (6) and apparent momentum source across all the grid scales are compared in Figure 12. Note that the detrainment term is estimated as the residual because the other three terms can be directly calculated from CRM data.

As shown in Figure 12a, apparent momentum source varies significantly with height and grid spacing for both updraft and downdrafts. For example, the  $x$ -component of updraft apparent momentum source ( $X_{xU}$ ) is positive and negative below and above 4 km height, respectively, with the maximum positive value at 3 km altitude for  $dx = 32 \sim 128$  km. The  $y$ -component of updraft apparent momentum source ( $X_{yU}$ ) is negative below 6 km but positive above 6 km height, with the

minimum  $X_{yU}$  occurring at  $\sim 5$  km altitude for  $dx = 32\sim 256$  km. Further, apparent momentum source in updrafts is larger than that in downdrafts ( $X_{xD}$  and  $X_{yD}$ ).

As shown in Eq. (6), the apparent momentum source is composed of CIPG, vertical advection of horizontal momentum, and detrainment (the three terms on the right-hand side of Eq. 6). The magnitudes of these three terms are much larger than that of apparent momentum source. The vertical advection of horizontal momentum has a slightly larger magnitude than that of CIPG and they are opposite in sign, except for the updraft  $y$ -component above 8 km altitude. The detrainment term is the smallest among the three terms. The magnitudes of CIPG and apparent momentum source are comparable at very large grid spacing such as 512 and 256 km. As grid spacing decreases, the magnitude of CIPG increases more rapidly than that of apparent momentum source, and thus CIPG becomes significantly larger than apparent momentum source at small grid spacings. These results suggest that CIPG can have significant impacts on apparent momentum source at GCM-resolution, and the impact may become even larger at the gray-zone resolution. Because of this finding, it is imperative to revisit the parameterization scheme for CIPG across all the scales.

To further understand the factors impacting the scale dependency of CIPG, vertical profiles of individual terms in the Laplacian of CIPG (Eq. 7) are compared for different grid spacings (Figures 13-14, and S8-S11). For MC3E-0523 (nonlinear MCS), contributions from the buoyancy, divergence, and stratification forcings to the Laplacian of CIPG are very small for all grid spacings (Figures 13 and S8-S9 in SI). Therefore, the discussion for MC3E-0523 will focus on the linear-shear and nonlinear-shear forcings below. For the  $x$ -component of both updraft and downdraft Laplacian of CIPG, the absolute value of the linear-shear forcing increases monotonically with decreasing grid spacing, and is the major contributor to the Laplacian of CIPG for all grid spacings



(Figures 13a and 13c). Although the linear-shear forcing has the same sign and similar vertical structures as the Laplacian of CIPG for all grid spacings, their differences in vertical profiles increase as the grid spacing increases.

Unlike the linear-shear forcing, the nonlinear-shear forcing has similar magnitudes across the grid spacings, and in general has the opposite sign to the Laplacian of CIPG and the linear-shear forcing. Because the linear-shear forcing's absolute value monotonically decreases with increasing grid spacing, contribution from the nonlinear-shear forcing to the Laplacian of CIPG becomes noticeable at  $dx = 32$  km and becomes comparable to the linear-shear forcing in magnitude at grid spacings  $> 64$  km. This explains the increased difference with increased grid spacing between the linear-shear forcing and the Laplacian of CIPG.

Different from the  $x$ -component for updraft and downdraft Laplacian of CIPG whose linear-shear forcing is always larger than the other four terms regardless of grid spacings, for the  $y$ -component of updraft and downdraft Laplacian of CIPG (Figures 13b and 13d), the nonlinear-shear forcing in its absolute value becomes larger than the linear-shear forcing at  $dx > 64$  km. In addition, the linear shear forcing term does not always have the same sign as the Laplacian of CIPG when  $dx > 16$  km, in particular at  $dx = 256$  and  $512$  km.

For MC3E-0520 (linear MCS), contributions from the divergence and stratification forcings to the Laplacian of CIPG remain negligibly small (Figure 14). For  $dx = 4\sim 64$  km, the  $x$ - and  $y$ -components of both updraft and downdraft linear-shear forcings in general have the same sign as the Laplacian of CIPG and are the major contributor to the Laplacian of CIPG. However, for  $dx=128\sim 512$  km, contributions of the linear-shear, nonlinear-shear, and buoyancy forcings to the Laplacian of CIPG become comparable, and the linear-shear forcing sometimes has an opposite sign to the Laplacian of CIPG below the 6 km altitudes.

The CIPG budget analysis presented above suggests that for both linear and nonlinear MCSs, both the nonlinear-shear forcing and/or buoyancy forcing become comparable to the linear-shear forcing and sometimes exceed the linear-shear forcing as the grid spacing increase from 4~64 km to 128~256 km although the linear-shear forcing is the major contributor to the Laplacian of CIPG for 4~64 km grid spacings. Thus, inclusion of the linear-shear forcing only to represent the Laplacian of CIPG such as in the GKI97 scheme may be acceptable only at  $dx = 4\text{-}64$  km where the magnitudes of other forcings are small.

#### **4.4 Scale dependency of parameterized CIPG by the GKI97 scheme**

The GKI97 scheme (Eq. 8) only includes the linear-shear forcing term for parameterizing CIPG, that is, a constant coefficient multiplied by mass flux and vertical mean wind shear. The same constant coefficient is used in the  $x$ - and  $y$ -components of CIPG for updrafts and downdrafts. As revealed from Figures 13 and 14, the relationship between CIPG and linear-shear forcing term can be different for the  $x$ - and  $y$ -components at different grid spacings. Thus, using the same coefficient for their  $x$ - and  $y$ -components across different grid spacings may cause significant errors. Although the stratification and divergence forcings are small and neglecting them is justifiable, contributions of both the nonlinear-shear and buoyancy forcings to CIPG are not negligible at  $dx > 64$  km. Thus, we suspect that exclusion of the nonlinear-shear forcing or buoyancy forcing in the parameterization of CIPG may impact the degree of accuracy. Therefore, in this section we evaluate the performance of the GKI97 scheme for parameterizing the CIPG for different grid spacings using the linear regression analysis at each level for different grid spacings.

Both MC3E-0520 and MC3E-0523 consistently show that at  $dx = 4 \sim 128$  km, the  $x$ - and  $y$ -component CIPG and product of mass flux and vertical mean wind shear for updrafts and downdrafts (Eq. 8) are negatively correlated at all levels, while for  $dx = 256$  and 512 km, they can

be either positively or negatively correlated (Figures 15 and S12). In addition,  $R_{adj}^2$  monotonically increases with increasing grid spacing at the 4~64 km range, in which the grid spacing of 64 km has the maximum  $R_{adj}^2$ . This suggests that the GKI97 scheme may explain the most CIPG variation at  $dx = 64$  km, and at the smaller the grid spacing the less variation of CIPG can be captured by the GKI97 scheme. In contrast, for  $dx > 64$  km, there is no such clear relation between  $R_{adj}^2$  and grid spacing, and  $R_{adj}^2$  varies greatly with height.

As for the regression slopes, it is shown that at the grid spacing ranging from 4 km to 128 km, the range of the slope variation in the vertical (1-12 km altitudes) tends to increase as grid spacing increases for both the  $x$ - and  $y$ -components of updrafts and downdrafts (Table 1 and Table S1 in SI). For example, for  $dx = 4$  km from MC3E-0523, the  $x$ -component of updraft slopes ranges from -0.44 to -0.24, and for  $dx = 128$  km, they range from -0.47 to -0.07. However, the mean slopes averaged over 1-12 km altitude do not vary much with grid spacings. The mean slopes are ranging from -0.32 to -0.37 across the grid spacings for the  $x$ -component of updraft slopes, from -0.32 to -0.41 for the  $y$ -component of updrafts slopes, from -0.45 to -0.49 for the  $x$ -component of downdraft slopes, and from -0.49 to -0.52 for the  $y$ -component of downdraft slopes. Since the mean regression slope does not vary much with grid spacing for the same component, we take vertical averages. The average slope is -0.35 for the  $x$ -component of updraft slope, -0.39 for the  $y$ -component of updraft slope, -0.47 for the  $x$ -component of downdraft slope, and -0.50 for the  $y$ -component of downdraft slope from MC3E-0523 (Table 2). The average slopes for MC3E-0520 is also listed in Table 2. It appears that the average slopes are different for different cases. In general, the average slopes appear to be larger for downdrafts than updrafts.

In summary, the two cases consistently demonstrate that the GKI97 scheme is satisfactory to a first-order approximation of parameterized CIPG for climate models with grid size of  $< 64$

km. However, the variations of CIPG that can be captured using the GKI97 scheme decrease when grid spacing increases. When grid spacing is at 128 km or larger, the GKI97 scheme does not fully parameterize CIPG. This behavior is related to the fact that GKI97 only considers the contribution from linear forcing, but does not consider the contribution from the nonlinear-shear forcing or buoyancy forcing, which can become comparable or even larger than the linear-shear forcing when  $dx > 64$  km. It is surprising that the GKI97 scheme is actually not suitable when the model grid spacing is at the traditional GCM scales (100-300 km). This might explain why Richter and Rasch (2008), which used horizontal resolutions of  $1.9^\circ$  and  $2.5^\circ$ , obtained better result from the SL76 scheme that did not consider the effect of CIPG than that from the GKI97 scheme that includes the CIPG effect.

To investigate whether adding the nonlinear shear forcing into the GKI97 scheme can potentially improve the ability for capturing the variation of CIPG, we conduct a multiple linear regression analysis using two predictor variables, including the product of mass flux and vertical mean wind shear (GKI97, linear-shear forcing) and the product of mass flux and vertical perturbation wind shear (nonlinear-shear forcing). It is shown that when nonlinear-shear term is added into the regression equation,  $R_{adj}^2$  value increases significantly at the  $dx = 128$ -512 km (Figure 16). However, the increase of  $R_{adj}^2$  value at  $dx < 100$  km is much smaller compared to that at  $dx > 100$  km. This confirms that adding the non-linear forcing to the GKI97 scheme might potentially improve the predictability of CIPG for  $dx > 100$  km, while the improvement is limited for  $dx < 100$  km. A potentially better way to parameterize the CIPG at the grid spacing range from 4 km to 64 km would still use the GKI97 scheme, but with a modification that can capture the large inter-draft variability in convective updraft area within a grid box. This may be achieved by using the three updrafts and one downdraft approach (Liu et al., 2015), which shows much

improved CMT compared to the traditional single updraft and downdraft approach as shown in Figure 17 because it well accounts for the increasing variation inside convection at the gray zone scale.

## **5. Summary and discussions**

This study has focused on diagnosing and exploring the scale dependency of convective momentum transport (CMT) and CMT-related properties, and evaluating the convection-induced pressure gradient (CIPG) parameterization in Gregory et al. 1997 (GKI97). A statistical ensemble method is used to analyze the 3-D Weather Research and Forecasting (WRF) model simulations at the cloud-permitting scale for two mid-latitude convective systems, i.e., a mesoscale convective complex and a squall line observed during the MC3E field experiment.

The two CRM-simulated cases consistently show that the grid-mean wind patterns generally do not change much with the change of grid spacings except for the y-component of the linear MCS. In contrast, updraft and downdraft mass fluxes and CMTs have strong scale dependency in temporal evolution and vertical structure. However, even with strong scale dependency, updraft CMT has the same sign from the small grid spacings to the large grid spacings, while downdraft CMT can have different signs between the small and large grid spacings.

Previous studies suggest that CMT is generally downgradient for nonlinear MCSs, but for linear MCSs, the CMT can be either upgradient or downgradient transports. We find that the prevalent CMT characteristics based upon field campaigns and model calculation for spatial scales typical of current GCM resolution are applicable to updrafts but not downdrafts across a wide range of grid spacings. Total and updraft CMT for the nonlinear MCSs (MC3E-0523) are mostly downgradient with respect to grid-mean wind shear at all levels for both the small and large grid spacings. Updraft and total CMT for the linear MCS (MC3E-0520) also consistently show

downgradient transport in the line-parallel direction and upgradient transport in the line-normal direction for both large grid spacings at all levels and small grid spacings below 7 km altitude. In contrast, downdraft CMT for nonlinear MCSs is upgradient at the large grid spacings and becomes downgradient at the small grid spacings. For linear MCS, downdraft CMT is mostly downgradient for both the  $x$ - and  $y$ -components at both the small and large spacings.

We also investigate why linear MCS has downgradient updraft CMT in the  $x$  direction but upgradient CMT in the  $y$  direction for both large and small grid spacings. For the upgradient CMT in the  $y$  direction, the reason is that the updraft pressure gradient force (PGF) strengthens perturbation wind in updrafts for both the large and small grid spacings. In contrast, in the  $x$  direction, the updraft PGF weakens perturbation wind inside updrafts, resulting in downgradient CMT. However, downdraft CMT shows no clear relation to downdraft PGF.

The analyses of scale dependency of apparent momentum source suggest that CIPG has significant impacts on apparent momentum source at GCM-resolution, and the influence becomes even larger at the gray-zone resolution. Further analysis of the individual components for the Laplacian of CIPG shows that although linear-shear forcing is the major contributor to the  $x$ -component of updraft and downdraft Laplacian of CIPG for all the grid spacings from MC3E-0523, the contribution of nonlinear shear forcing to the  $y$ -component of updraft and downdraft Laplacian of CIPG from MC3E-0523 as well as both the  $x$ - and  $y$ -components of Laplacian of CIPG from MC3E-0520 can be comparable and even exceeds the linear-shear forcing at grid spacing larger than 64 km. This suggest that use of only the linear-shear forcing for representing the Laplacian of CIPG might be acceptable only at  $dx = 4\sim 64$  km either when convective scale effect dominates or when the mesoscale circulation is absent. However, when grid spacing is large,

the effect of MCS organization is inevitable to be included in each grid box, and thus the inclusion of the no-linear-shear forcing becomes important.

We have also evaluated one of the most widely used CMT parameterization schemes in GCMs that included the effect of CIPG [Wu and Yanni 1994; Gregory et al., 1997, GKI97]. We performed the linear regression analysis between the CIPG and the product of mass flux and vertical mean wind shear at each level to quantify the performance of the GKI97 scheme across different grid spacings. Results show that  $R_{adj}^2$  monotonically increases with increasing grid spacing at the grid spacing range between 4 km and 64 km, in which the grid spacing of 64 km has the maximum  $R_{adj}^2$ . This suggests that the GKI97 scheme may explain the most CIPG variation at grid spacing of 64 km, and at the smaller the grid spacing, the less variation of CIPG can be captured by the GKI97 scheme. Based on the multiple-variable regression analysis, the ability to capture the increasing variation of CIPG with decreasing grid spacing cannot be improved with the inclusion of nonlinear shear forcing as another predictor. Thus, a better way to parameterize the convection-induced pressure gradient at the grid spacing range from 4 km to 64 km would still use the GKI97 scheme, but with a modification that can capture the large inter-draft variability in convective updraft area within a grid box. This may be achieved by using the three updrafts approach (Liu et al., 2015), which can well account for the increasing variation inside convection at the gray zone scale compared to the traditional single updraft and downdraft approach.

We also found that when grid spacing increases to 128 km or larger, the negative correlation between CIPG and the linear-shear forcing would somehow break down and becomes highly sensitive to altitudes. This is because the GKI97 scheme does not consider the contribution from the nonlinear shear forcing and buoyancy forcing, which can be comparable or even larger than the linear-shear forcing when  $dx$  is larger than 100 km. This finding suggests that the GKI97

696 parametrization for CIPG is actually not suitable for model grid spacing at the traditional GCM  
697 scales (100-300 km) unless the non-linear forcing is included.



698 **Acknowledgments:**

699         Support for this work was provided by Scientific Discovery through Advanced Computing  
700 (SciDAC) program funded by U.S. Department of Energy Office of Advanced Scientific  
701 Computing Research and Office of Biological and Environmental Research. The Pacific  
702 Northwest National Laboratory (PNNL) is operated for the DOE by Battelle Memorial Institute  
703 under contract DE-AC06-76RLO 1830. Kuan-Man Xu was supported by NASA Modeling,  
704 Analysis and Prediction program. Guang J. Zhang was supported by the PNNL SciDAC  
705 subcontract DOE/PNNL 190110. The data used in this study were produced by Pacific Northwest  
706 National Laboratory (PNNL), and are stored on PNNL Olympus. They are available upon request  
707 by contacting the corresponding author.

708

## Reference

- Arakawa, A., and C.-M. Wu, 2013: A unified representation of deep moist convection in numerical modeling of the atmosphere. Part I. *J. Atmos. Sci.*, **70**, 1977–1992.
- , J.-H. Jung, and C.-M. Wu, 2011: Toward unification of the multiscale modeling of the atmosphere. *Atmos. Chem. Phys.*, **11**, 3731–3742.
- Asai, T., 1970: Three-dimensional features of thermal convection in a plane Couette flow. *J. Meteor. Soc. Japan*, **48**, 18–29.
- Cheng, A., and K.-M. Xu., 2014: An explicit representation of vertical momentum transport in a multiscale modeling framework through its 2-D cloud-resolving model component. *J. Geophys. Res.*, **119**, 2356–2374.
- Deng, L., and X. Wu, 2010: Effects of Convective Processes on GCM Simulations of the Madden–Julian Oscillation. *J. Climate*, **23**, 352–377.
- Fan, J., L. R. Leung, Z. Li, H. Morrison, H. Chen, Y. Zhou, Y. Qian, and Y. Wang, 2012: Aerosol impacts on clouds and precipitation in eastern China: Results from bin and bulk microphysics. *J. Geophys. Res.*, **117**, D00K36, doi:10.1029/2011JD016537.
- , Y.-C. Liu, K.-M. Xu, K. North, S. Collis, X. Dong, G.J. Zhang, Q. Chen, P. Kollias, and S.J. Ghan, 2015: Improving representation of convective transport for scale-aware parameterization: 1. Convection and cloud properties simulated with spectral bin and bulk microphysics. *J. Geophys. Res. Atmos.*, **120**, 3485–3509. doi: 10.1002/2014JD022142.
- Gallus, W. A., Jr., and R. H. Johnson, 1992: The momentum budget of an intense midlatitude squall line. *J. Atmos. Sci.*, **49**, 422–450.

731 Grabowski, W. W., and M. W. Moncrieff, 2001: Largescale organization of tropical convection  
732 in two dimensional explicit numerical simulations. *Q. J. R. Meteorol. Soc.*, **127**, 445–468.

733 Gregory, D., R. Kershaw, and P. M. Inness, 1997: Parameterization of momentum transport by  
734 convection. II: Tests in single-column and general circulation models. *Quart. J. Roy.  
735 Meteor. Soc.*, **123**, 1153–1183.

736 Han, J. and H.-L. Pan, 2006: Sensitivity of Hurricane Intensity Forecast to Convective Momentum  
737 Transport Parameterization. *Mon. Wea. Rev.*, **134**, 664–674.

738 Helfand, H. M., 1979: The effect of cumulus friction on the simulation of the January Hadley  
739 circulation by the GLAS model of the general circulation. *J. Atmos. Sci.*, **36**, 1827–1843.

740 Houze, R. A., Jr., 1973: A climatological study of vertical transports by cumulus-scale  
741 convection. *J. Atmos. Sci.*, **30**, 1112–1123.

742 Houze, R.A., S.S. Chen, D.E. Kingsmill, Y. Serra, and S.E. Yuter, 2000: Convection over the  
743 Pacific Warm Pool in relation to the Atmospheric Kelvin-Rossby Wave. *J. Atmos.*  
744 *Sci.*, **57**, 3058–3089.

745 Khain, A., A. Pokrovsky, M. Pinsky A. Seifert, and V. Phillips, 2004: Simulation of effects of  
746 atmospheric aerosols on deep turbulent convective clouds using a spectral microphysics  
747 mixed-phase cumulus cloud model. Part I: Model description and possible applications. *J.*  
748 *Atmos. Sci.*, **61**, 2963–2982.

749 Khairoutdinov, M. F., and D. A. Randall, 2001: A cloud resolving model as a cloud  
750 parameterization in the NCAR Community Climate Model: Preliminary results. *Geophys.*  
751 *Res. Lett.*, **28**, 3617–3620.

752 Khouider, B., Y. Han, and J.A. Biello, 2012a: Convective Momentum Transport in a Simple  
 753 Multicloud Model for Organized Convection. *J. Atmos. Sci.*, **69**, 281–302.

754 ———, and ———, A.J. Majda, and S.N. Stechmann, 2012b: Multiscale Waves in an MJO  
 755 Background and Convective Momentum Transport Feedback. *J. Atmos. Sci.*, **69**, 915–  
 756 933.

757 Lane, T.P. and M.W. Moncrieff, 2010: Characterization of Momentum Transport Associated  
 758 with Organized Moist Convection and Gravity Waves. *J. Atmos. Sci.*, **67**, 3208–  
 759 3225, <https://doi.org/10.1175/2010JAS3418.1>

760 LeMone, M. A., and D. P. Jorgensen, 1991: Precipitation and kinematic structure of an oceanic  
 761 mesoscale convective system. Part 11: Momentum transport and generation. *Mon. Wea.*  
 762 *Rev.*, **119**, 2639–2653.

763 ———, 1983: Momentum transport by a line of cumulonimbus. *J. Atmos. Sci.*, **40**, 1815–1834.

764 ———, G. M. Barnes, and E. J. Zipser, 1984: Momentum flux by lines of cumulonimbus over the  
 765 tropical ocean. *J. Atmos. Sci.*, **41**, 1914–1932.

766 ———, and M. W. Moncrieff, 1994: Momentum and mass transport by convective bands:  
 767 Comparisons of highly idealized dynamical models to observations. *J. Atmos. Sci.*, **51**,  
 768 281–305.

769 Liu, Y.-C., J. Fan, G.J. Zhang, K.-M. Xu, and S.J. Ghan, 2015: Improving representation of  
 770 convective transport for scale-aware parameterization: 2. Analysis of cloud-resolving  
 771 model simulations. *J. Geophys. Res. Atmos.*, **120**, 3510–3532.  
 772 doi: 10.1002/2014JD022145.

773 Majda, A. J., and S. N. Stechmann, 2008: Stochastic models for convective momentum  
 774 transport. *Proc. Natl. Acad. Sci. USA*, **105**, 17 614–17 619  
 775 ———, and ———, 2009: A Simple Dynamical Model with Features of Convective Momentum  
 776 Transport. *J. Atmos. Sci.*, **66**, 373–392, <https://doi.org/10.1175/2008JAS2805.1>  
 777 ———, and ———, 2016: Models for Multiscale Interactions. Part II: Madden–Julian Oscillation,  
 778 Moisture, and Convective Momentum Transport. *Meteorological Monographs*, **56**, 10.1–  
 779 10.5, <https://doi.org/10.1175/AMSMONOGRAPHIS-D-15-0005.1>  
 780 Moncrieff, M. W., and J. S. A. Green, 1972: The propagation and transfer properties of steady  
 781 convective overturning in shear. *Quart. J. Roy. Meteor. Soc.*, **98**, 336–352.  
 782 ———, 1992: Organized convective systems: Archetypal dynamical models, mass and momentum  
 783 flux theory, and parameterization. *Quart. J. Roy. Meteor. Soc.*, **118**, 819–  
 784 850.  
 785 ———, and C. Liu, 2006: Representing convective organization in prediction model by a hybrid  
 786 strategy. *J. Atmos. Sci.*, **63**, 3404–3420.  
 787 ———, 1981: A theory of organized steady convection and its transport properties. *Q.J.R. Meteorol.*  
 788 *Soc.*, **107**, 29–50.  
 789 ———, 1992: Organized convective systems: Archetypal dynamical models, mass and momentum  
 790 flux theory, and parameterization. *Quart. J. Roy. Meteor. Soc.*, **118**, 819–  
 791 850.  
 792 Neale, R. B., et al., 2010: Description of the NCAR Community Atmosphere Model (CAM5).  
 793 *Technical Report NCAR/TN-486+STR*, 268 pp, National Center for Atmospheric Research,  
 794 Boulder, Colo.

795 Ooyama, K., 1971: A theory on parameterization of cumulus convection. *J. Meteor. Soc. Japan*,  
796 **49**, 744–756.

797 Petersen, W. A., and M. Jensen, 2012: The NASA-GPM and DOE-ARM Midlatitude  
798 Continental Convective Clouds Experiment (MC3E). *Int. J. Appl. Earth Obs.*, **24**, 12–18,  
799 [http://pmm.nasa.gov/sites/default/files/document\\_files/Earth\\_Observer\\_Jan\\_2012\\_MC3E](http://pmm.nasa.gov/sites/default/files/document_files/Earth_Observer_Jan_2012_MC3E.pdf)  
800 [.pdf](http://pmm.nasa.gov/sites/default/files/document_files/Earth_Observer_Jan_2012_MC3E.pdf).

801 Rotunno, R. and J.B. Klemp, 1982: The Influence of the Shear Induced Pressure Gradient On  
802 Thunderstorm Motion. *Mon. Wea. Rev.*, **110**, 136–151.

803 Richter, J. H., and P. J. Rasch, 2008: Effects of Convective Momentum Transport on the  
804 Atmospheric Circulation in the Community Atmosphere Model, Version 3. *J.*  
805 *Climate*, **21**, 1487–1499.

806 Romps, D. M., 2012: On the Equivalence of Two Schemes for Convective Momentum  
807 Transport. *J. Atmos. Sci.*, **69**, 3491–3500.

808 Schneider, E. K., and R. S. Lindzen, 1976: A discussion of the parameterization of momentum  
809 exchange by cumulus convection. *J. Geophys. Res.*, **81**, 3158–3161.

810 Shapiro, L.J. and D.E. Stevens, 1980: Parameterization of Convective Effects on the Momentum  
811 and Vorticity Budgets of Synoptic-Scale Atlantic Tropical Waves. *Mon. Wea.*  
812 *Rev.*, **108**, 1816–1826.

813 Shaw, T.A. and T.P. Lane, 2013: Toward an Understanding of Vertical Momentum Transports in  
814 Cloud-System-Resolving Model Simulations of Multiscale Tropical Convection. *J. Atmos.*  
815 *Sci.*, **70**, 3231–3247, <https://doi.org/10.1175/JAS-D-13-068.1>

816 Song, X., X. Wu, G. J. Zhang, and R. W. Arritt, 2008: Dynamical Effects of Convective  
817 Momentum Transports on Global Climate Simulations. *J. Climate*, **21**, 180–194.

818 Sui, C.-H., and M. Yanai, 1986: Cumulus ensemble effects on the large-scale vorticity and  
819 momentum fields of GATE. Part I: Observational evidence. *J. Atmos. Sci.*, **43**, 1628-1642.

820 Tollerud, E. I., and S. K. Esbensen, 1983: An observational study of the upper-tropospheric  
821 vorticity fields in GATE cloud clusters. *Mon. Wea. Rev.*, **111**, 2161-2175.

822 Tulich, S. N., 2015: A strategy for representing the effects of convective momentum transport in  
823 multiscale models: Evaluation using a new superparameterized version of the Weather  
824 Research and Forecast model (SP-WRF). *J. Adv. Model. Earth Syst.*, **7**, 938–962,  
825 doi:[10.1002/2014MS000417](https://doi.org/10.1002/2014MS000417).

826 Tung, W.-W., and M. Yanai, 2002a: Convective momentum transport Observed during the TOGA  
827 COARE IOP. Part I: General features. *J. Atmos. Sci.*, **59**, 1857–1871.

828 ———, and ———, 2002b: Convective Momentum Transport Observed during the TOGA COARE  
829 IOP. Part II: Case Studies. *J. Atmos. Sci.*, **59**, 2535–2549.

830 Wang, Y., J. Fan, R. Zhang, L. R. Leung, and C. Franklin, 2013: Improving bulk microphysics  
831 parameterizations in simulations of aerosol effects. *J. Geophys. Res. Atmos.*, **118**, 5361–  
832 5379, doi:[10.1002/jgrd.50432](https://doi.org/10.1002/jgrd.50432)

833 Wu, C.-M., and A. Arakawa, 2014: A Unified Representation of Deep Moist Convection in  
834 Numerical Modeling of the Atmosphere. Part II. *J. Atmos. Sci.*, **71**, 2089–2103.

835 Wu, X., and M. Yanai, 1994: Effects of vertical wind shear on the cumulus transport of  
836 momentum: Observations and parameterization. *J. Atmos. Sci.*, **51**, 1640–1660.

837 ———, X. Liang, and G. J. Zhang, 2003: Seasonal migration of ITCZ precipitation across the  
838 equator: Why can't GCMs simulate it? *Geophys. Res. Lett.*, **30**(15), 1824,  
839 doi:[10.1029/2003GL017198](https://doi.org/10.1029/2003GL017198).

840 Zhang, G. J. and H. R. Cho, 1991a: Parameterization of the vertical transport of momentum by  
841 cumulus clouds. Part I: Theory. *J. Atmos. Sci.*, **48**, 1483-1492.  
842 ———, and ———, 1991b: Parameterization of the vertical transport of momentum by cumulus clouds.  
843 Part II: Application. *J. Atmos. Sci.*, **48**, 2448-2457.  
844 ———, and X. Wu, 2003: Convective momentum transport and perturbation pressure field from a  
845 cloud-resolving model simulation. *J. Atmos. Sci.*, **60**, 1120–1139.  
846 ———, and N. A. McFarlane, 1995: Role of convective-scale momentum transport in climate  
847 simulation. *J. Geophys. Res.*, **100**, 1417–1426.  
848



## Figure captions

Figure 1. Time-height cross sections of grid-mean (a) x component winds ( $\bar{u}$ ,  $\text{m}^{-1} \text{s}^{-1}$ ) and (b) y component winds ( $\bar{v}$ ,  $\text{m}^{-1} \text{s}^{-1}$ ) averaged over the ensemble domains at  $\text{dx} = 8 \text{ km}$  and  $\text{dx} = 128 \text{ km}$  for MC3E-0523. Time period is from 1930 UTC 23 May to 0130 UTC 24 May. Please refer to Fig. S1 (Supporting Information) for the results of all different grid spacings.

Figure 2. Same as Figure 1, except from MC3E-0520. Time period is from 1300 UTC 20 May to 1700 UTC 20 May. Please refer to Fig. S2 (Supporting Information) for the results of all different grid spacings.

Figure 3 Snapshots of the grid-mean y component winds ( $\text{m}^{-1} \text{s}^{-1}$ ) at 6.0 km altitude at 1400 UTC 20 May for (a)  $\text{dx} = 8 \text{ km}$  and (b)  $\text{dx} = 128 \text{ km}$  for MC3E-0520. (c) shows the snapshot of updraft points (red) and downdraft points (blue) at the same height and time from the CRM simulation with 1-km grid-spacing.

Figure 4. Time-height cross sections of ensemble mean mass flux ( $\text{kg m}^{-2} \text{s}^{-1}$ ) in (a) convective updrafts and (b) downdrafts for  $\text{dx} = 8 \text{ km}$  and  $\text{dx} = 128 \text{ km}$  from MC3E-0523. Time period is from 1930 UTC 23 May to 0130 UTC 24 May. Please refer to Fig. S3 for the results of all different grid spacings.

Figure 5. Time-height cross sections of the x component of ensemble mean vertical momentum flux ( $\text{kg m}^{-1} \text{s}^{-2}$ ) in (a) convective updrafts and (b) downdrafts for  $\text{dx} = 8 \text{ km}$  and  $\text{dx} = 128 \text{ km}$  from MC3E-0523. Time period is from 1930 UTC 23 May to 0130 UTC 24 May. Please refer to Fig. S4 for the results of all different grid spacings.

Figure 6. Same as Figure 5, except for y component of ensemble mean vertical momentum flux ( $\text{kg m}^{-1} \text{s}^{-2}$ ). Please refer to Fig. S5 for the results of all different grid spacings.

Figure 7. Vertical profiles of the ensemble mean of the convective momentum fluxes and grid-mean vertical wind shear for (a) MCE3-0523 and (b) MC3E-0520. The red, blue, and black solid lines denote updraft, downdrafts, and total convective momentum fluxes, respectively, with the scale shown at the bottom of each frame. The green-dotted line is for grid-mean vertical wind shear with the scale shown at the top of each frame. The left two frames are x component, and the right two frames are y component at  $\text{dx} = 8 \text{ km}$  and  $128 \text{ km}$ .

Figure 8. The horizontal cross section of the x component of updraft convective momentum flux ( $\text{kg m}^{-1} \text{s}^{-2}$ ) (a, c, and e) and updraft pressure gradient force ( $\text{m s}^{-2}$ ) (b, d, and f) for  $\text{dx} = 128 \text{ km}$  (the first row) and  $\text{dx} = 8 \text{ km}$  (the second and third rows) at 4.5 km altitudes at 1400 UTC 20 May. (e) and (f) are the closer look of black box in (c) and (d), respectively.

890 Figure 9. Same as Figure 8, except for x component at 9 km altitude.

891 Figure 10. Same as Figure 8, except for y component at 4.5 km altitude.

892 Figure 11. Same as Figure 8, except for y component at 7.5 km altitude.

893 Figure 12. Vertical profiles of scale dependency of (a) apparent momentum source ( $\text{m s}^{-1} \text{day}^{-1}$ ),  
894 (b) CIPG ( $\text{m s}^{-1} \text{day}^{-1}$ ), (c) vertical advection by the compensating subsidence ( $\text{m s}^{-1} \text{day}^{-1}$ ), and (d)  
895 horizontal momentum detrainment ( $\text{m s}^{-1} \text{day}^{-1}$ ) for MC3E-0523. The panels from left to right are  
896 x component of updrafts, y component of updrafts, x component of downdrafts, and y component  
897 of downdrafts, respectively.

898 Figure 13. Linear-shear forcing (black line,  $10^{-11} \text{kg m}^{-4} \text{s}^{-2}$ ), nonlinear-shear forcing (blue line,  $10^{-11} \text{kg m}^{-4} \text{s}^{-2}$ ),  
899 stratification forcing (green line,  $10^{-11} \text{kg m}^{-4} \text{s}^{-2}$ ), divergence forcing (red line,  $10^{-11} \text{kg m}^{-4} \text{s}^{-2}$ ), buoyancy forcing (yellow line,  $10^{-11} \text{kg m}^{-4} \text{s}^{-2}$ ), and the Laplacian of CIPG (black line with  
900 asterisk markers) over (a) x component of updrafts, (b) y component of updrafts, (c) x component  
901 of downdrafts, and (d) y component of downdrafts for MC3E-0523. Please refer to Figs. S8 and  
902 S9 for the results of all different grid spacings.

904

905 Figure 14. Same as Figure 13, except for MC3E-0520. Please refer to Figs. S10 and S11 for the  
906 results of all different grid spacings.

907 Figure 15. Vertical profiles of Pearson correlation coefficient (CC), adjusted coefficient of  
908 determination ( $R_{adj}^2$ ), and linear regression slope between CIPG and the product of mass flux  
909 and the vertical mean wind shear for (a) x component of updrafts, (b) y component of updrafts,  
910 (c) x component of downdrafts, and (d) y component of downdrafts from MC3E-0523. The  
911 hollow dots indicate where CC,  $R_{adj}^2$ , and linear regression slope are statistically insignificant.

912 Figure 16. Vertical profiles of  $R_{adj}^2$  for product of mass flux and vertical perturbation wind shear  
913 (left column), the combination of product of mass flux and vertical mean wind shear as well as  
914 product of mass flux and vertical perturbation wind shear (middle column) as predictor variables  
915 with CIPG as response variable. The difference in  $R_{adj}^2$  between the middle columns in Figures 15  
916 and 16 is also shown in the right column for (a) x component of updrafts, (b) y component of  
917 updrafts, (c) x component of downdrafts, and (d) y component of downdrafts from MC3E-0523.  
918 The hollow dots indicate where coefficients of determination are statistically insignificant.

919

920 Figure 17. Vertical profiles of the scale dependency of the x component of updraft vertical  
921 momentum flux ( $\text{kg m}^{-1} \text{s}^{-2}$ ) from CRM, the one-updraft approach, and the three-updraft approach  
922 for MC3E-0523. Please refer to Figs. S14 and S15 for the results of x, y components of updraft,  
923 downdraft, environment and total vertical momentum fluxes.

924

925

Table 1 The minimum, maximum, and average x component of updraft slopes (xU), y component of updraft slopes (yU), x component of downdraft slopes (xD), and y component of downdraft slopes (yD) between 1 km and 12 km heights for selected grid spacings from (a) MC3E-0523 and (b) MC3E-0520. For the results of all different grid spacings, please refer to Table S1.

(a) MC3E-0523

	xU			yU			xD			yD		
dx	min	max	avg	min	max	avg	min	max	avg	min	max	avg
8	-0.5	-0.22	-0.34	-0.48	-0.27	-0.38	-0.55	-0.16	-0.45	-0.67	-0.14	-0.49
128	-0.47	-0.07	-0.33	-0.62	-0.05	-0.32	-1.04	-0.07	-0.45	-0.9	-0.22	-0.51

(b) MC3E-0520

	xU			yU			xD			yD		
dx	min	max	avg	min	max	avg	min	max	avg	min	max	avg
8	-0.38	-0.17	-0.26	-0.54	-0.13	-0.39	-0.68	-0.28	-0.51	-0.63	-0.3	-0.48
128	-0.36	-0.12	-0.22	-0.86	0.25	-0.45	-0.48	-0.05	-0.32	-0.78	0.28	-0.23

935 Table 2. The mean of average x component of updraft slopes (xU), y component of updraft slopes  
 936 (yU), x component of downdraft slopes (xD), and y component of downdraft slopes (yD) from  
 937 Table S1 for MC3E-0523 and MC3E-0520.

	xU	yU	xD	yD
MC3E-0523	-0.35	-0.39	-0.47	-0.50
MC3E-0520	-0.27	-0.41	-0.42	-0.47

938

939

940

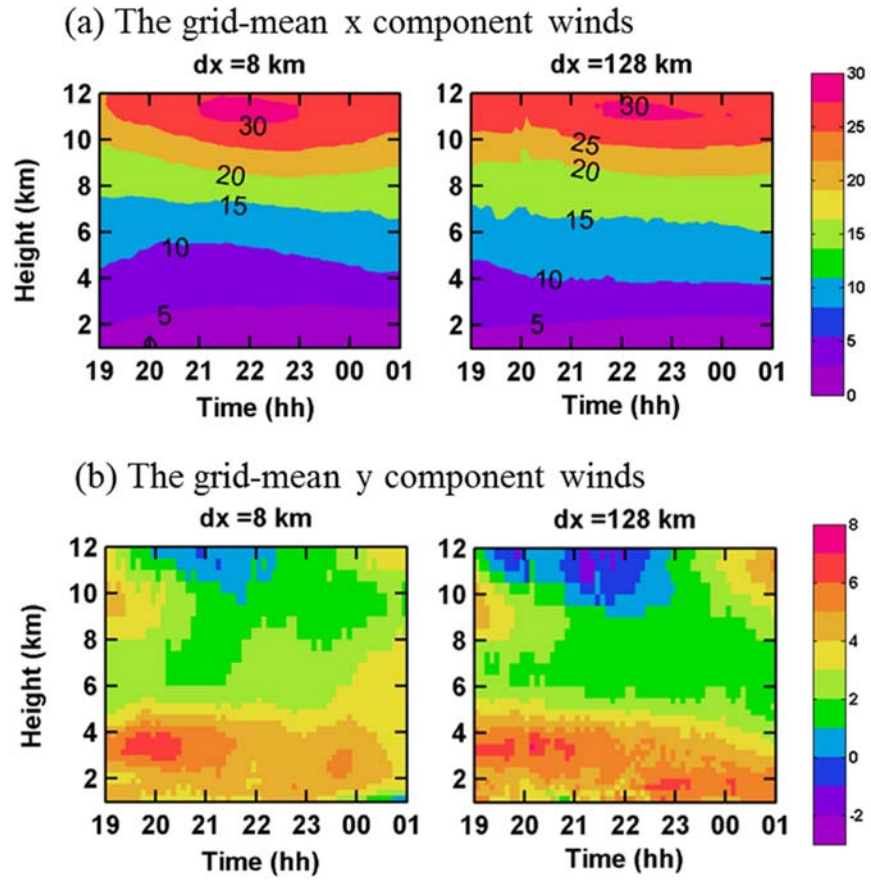


Figure 1. Time-height cross sections of grid-mean (a) x component winds ( $\bar{u}$ ,  $\text{m}^{-1} \text{s}^{-1}$ ) and (b) y component winds ( $\bar{v}$ ,  $\text{m}^{-1} \text{s}^{-1}$ ) averaged over the ensemble domains at  $dx = 8 \text{ km}$  and  $dx = 128 \text{ km}$  for MC3E-0523. Time period is from 1930 UTC 23 May to 0130 UTC 24 May. Please refer to Fig. S1 (Supporting Information) for the results of all different grid spacings.

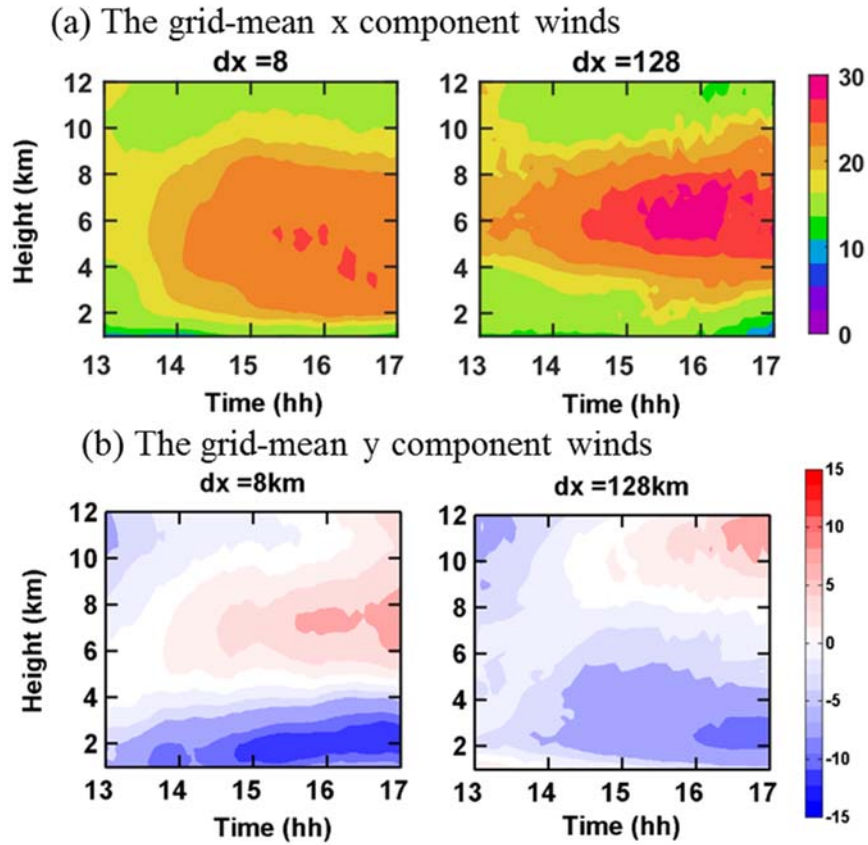


Figure 2. Same as Figure 1, except from MC3E-0520. Time period is from 1300 UTC 20 May to 1700 UTC 20 May. Please refer to Fig. S2 (Supporting Information) for the results of all different grid spacings.

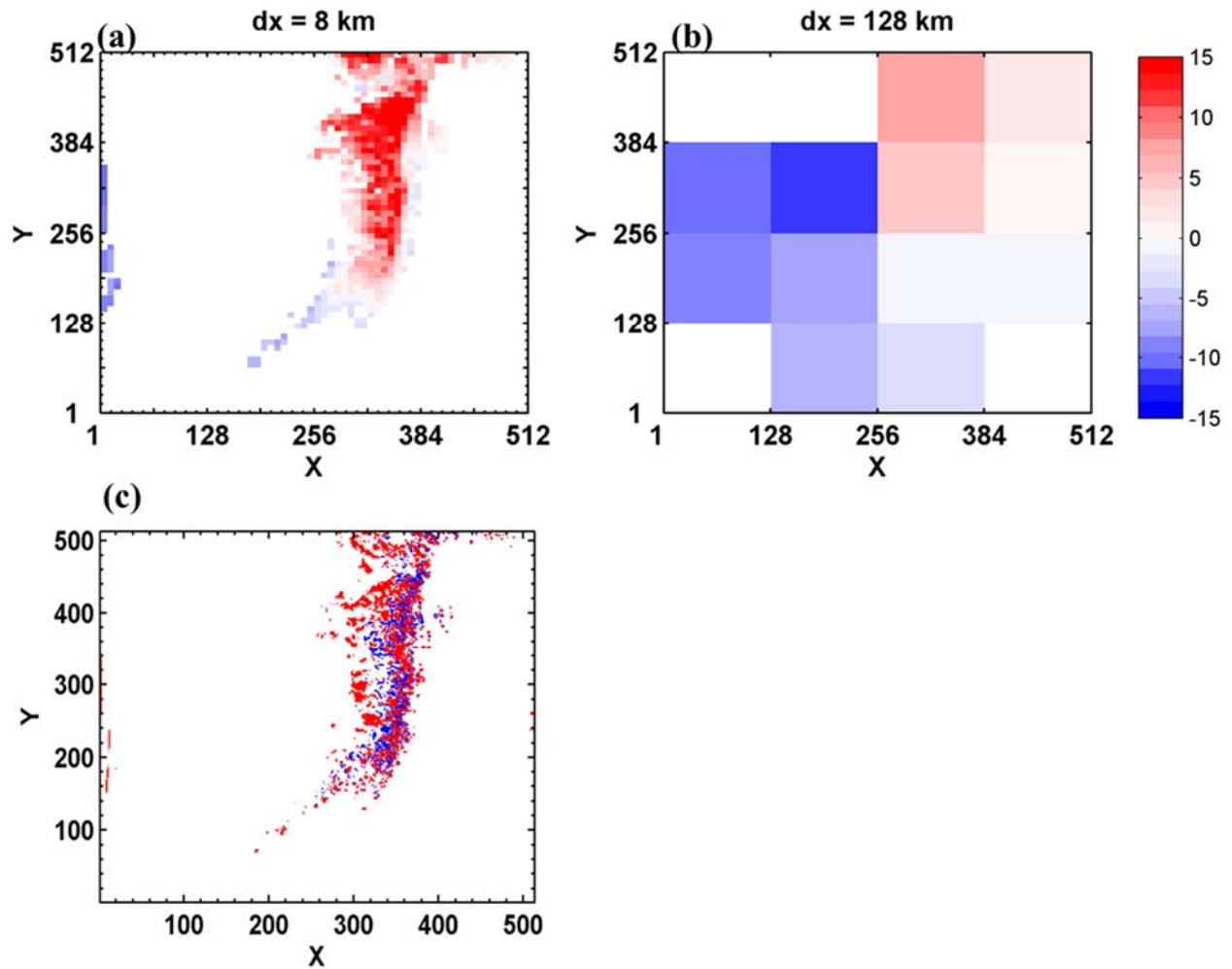
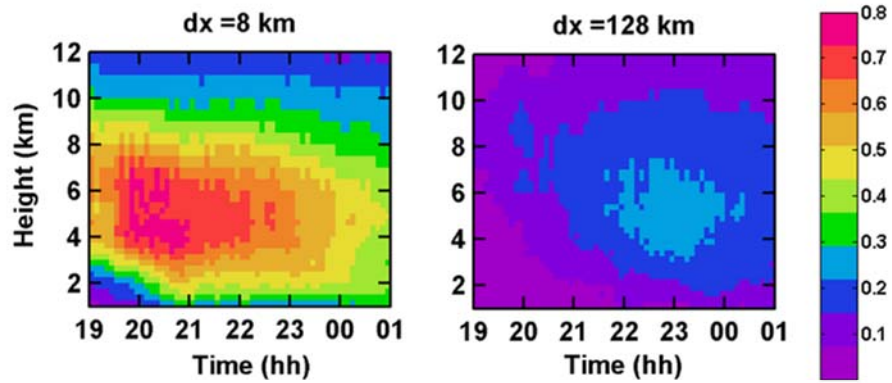
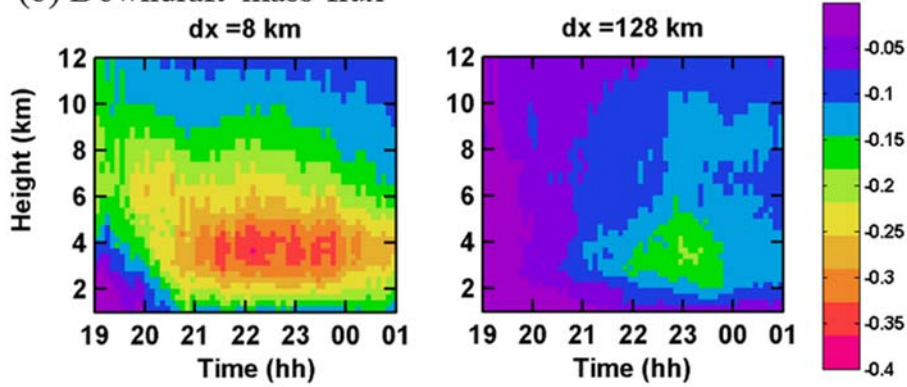


Figure 3 Snapshots of the grid-mean y component winds ( $\text{m}^{-1} \text{s}^{-1}$ ) at 6.0 km altitude at 1400 UTC 20 May for (a)  $dx = 8$  km and (b)  $dx = 128$  km for MC3E-0520. (c) shows the snapshot of updraft points (red) and downdraft points (blue) at the same height and time from the CRM simulation with 1-km grid-spacing.

(a) Updraft mass flux



(b) Downdraft mass flux



959

960 Figure 4. Time-height cross sections of ensemble mean mass flux ( $\text{kg m}^{-2} \text{s}^{-1}$ ) in (a) convective  
 961 updrafts and (b) downdrafts for  $dx = 8 \text{ km}$  and  $dx = 128 \text{ km}$  from MC3E-0523. Time period is  
 962 from 1930 UTC 23 May to 0130 UTC 24 May. Please refer to Fig. S3 for the results of all different  
 963 grid spacings.

964

965



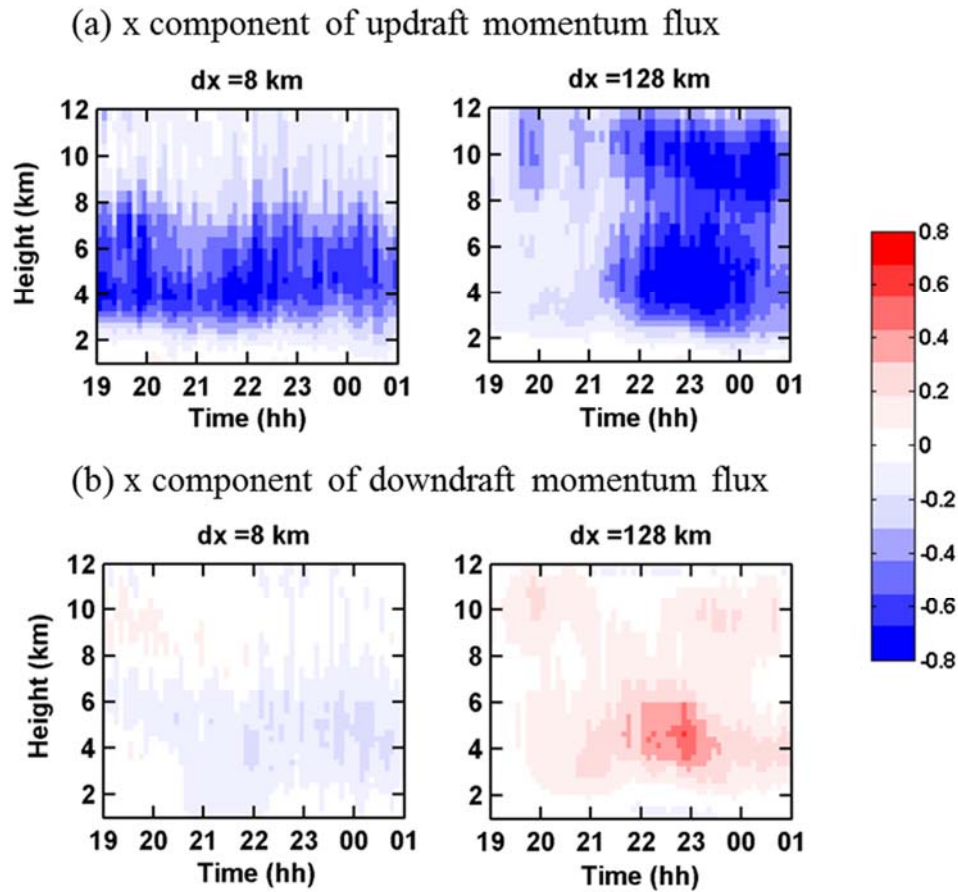
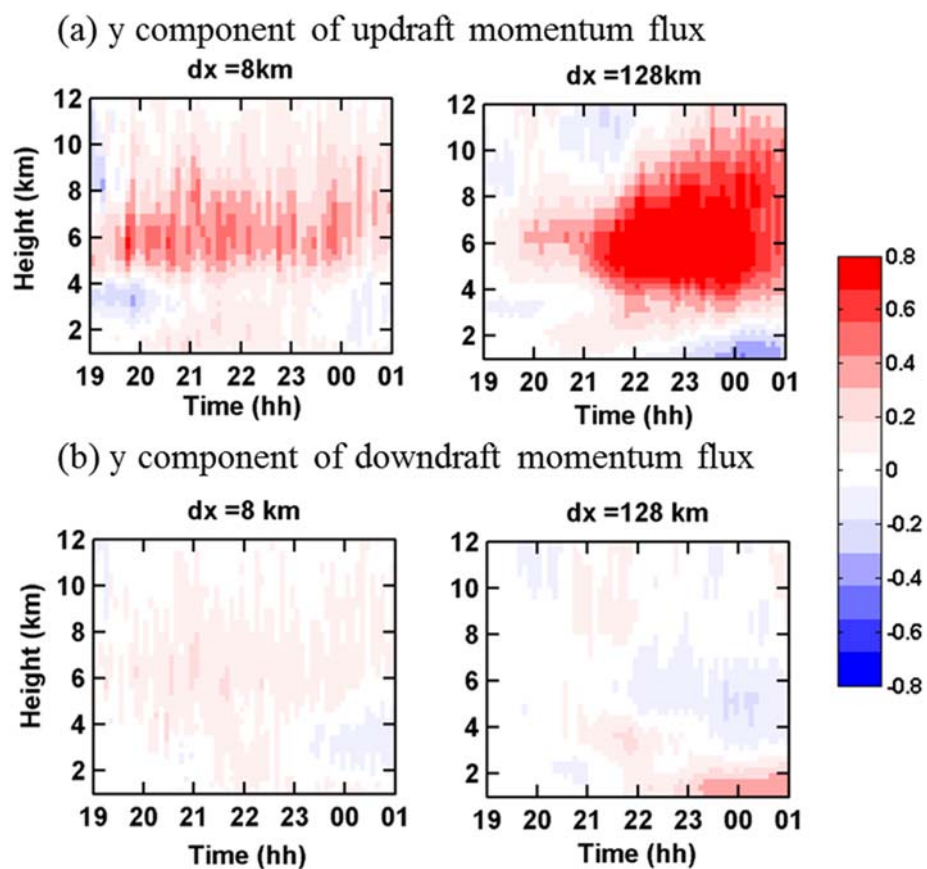


Figure 5. Time-height cross sections of the x component of ensemble mean vertical momentum flux ( $\text{kg m}^{-1} \text{s}^{-2}$ ) in (a) convective updrafts and (b) downdrafts for  $dx = 8 \text{ km}$  and  $dx = 128 \text{ km}$  from MC3E-0523. Time period is from 1930 UTC 23 May to 0130 UTC 24 May. Please refer to Fig. S4 for the results of all different grid spacings.



974  
 975 Figure 6. Same as Figure 5, except for y component of ensemble mean vertical momentum flux  
 976 ( $\text{kg m}^{-1} \text{s}^{-2}$ ). Please refer to Fig. S5 for the results of all different grid spacings.  
 977

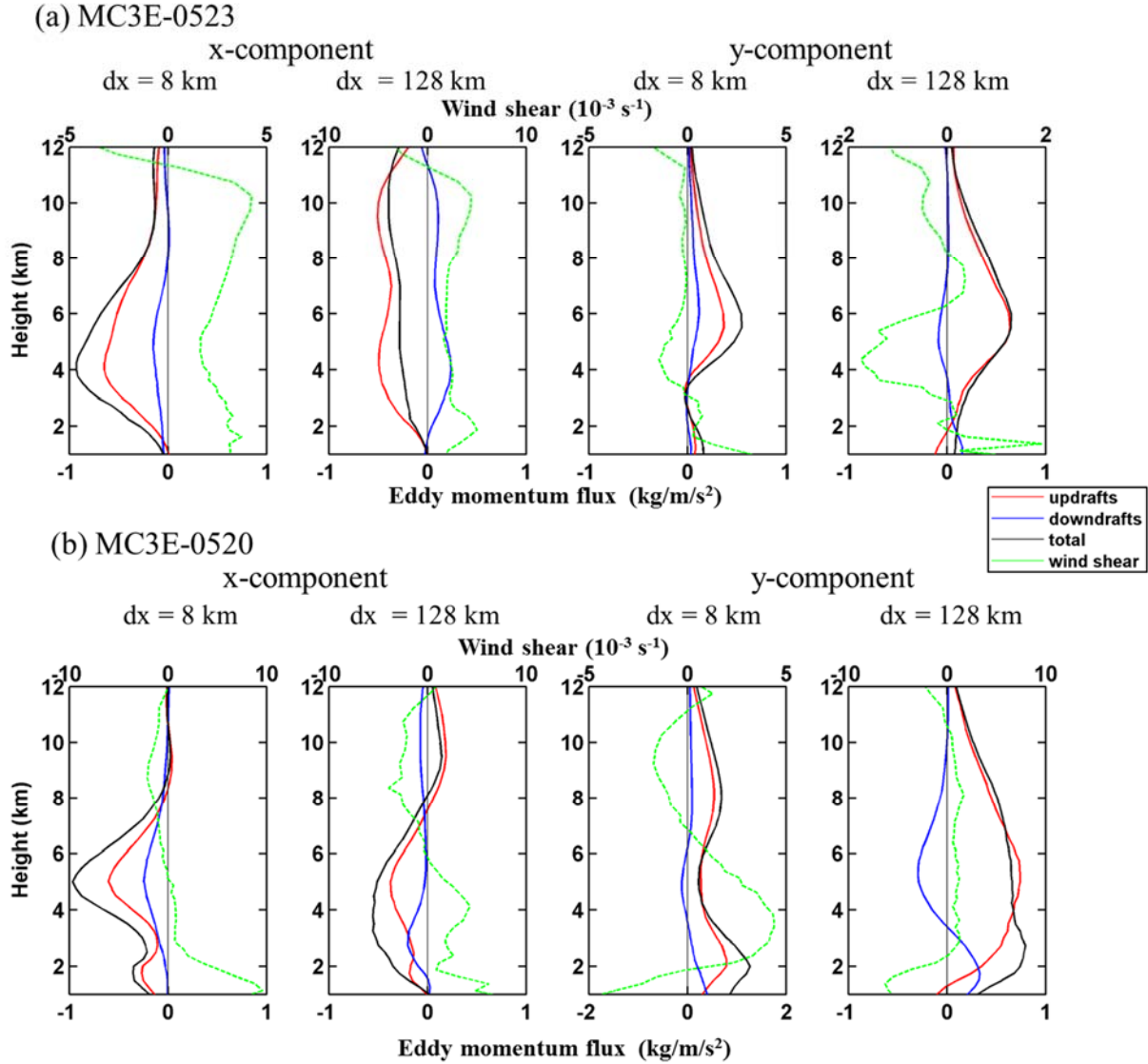


Figure 7. Vertical profiles of the ensemble mean of the convective momentum fluxes and grid-mean vertical wind shear for (a) MCE3-0523 and (b) MC3E-0520. The red, blue, and black solid lines denote updraft, downdrafts, and total convective momentum fluxes, respectively, with the scale shown at the bottom of each frame. The green-dotted line is for grid-mean vertical wind shear with the scale shown at the top of each frame. The left two frames are x component, and the right two frames are y component at  $dx = 8 \text{ km}$  and  $128 \text{ km}$ .

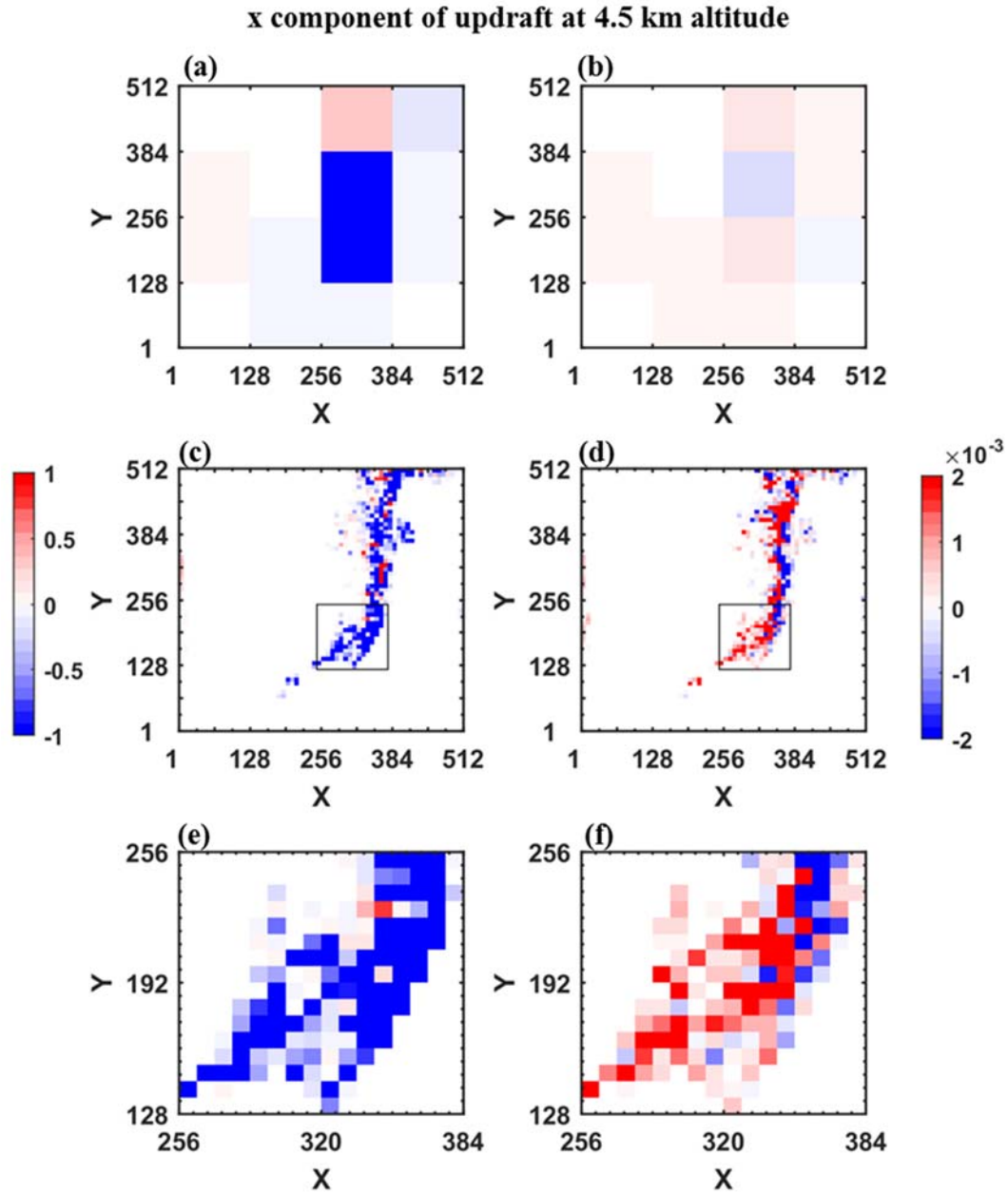


Figure 8. The horizontal cross section of the x component of updraft convective momentum flux ( $\text{kg m}^{-1} \text{s}^{-2}$ ) (a, c, and e) and updraft pressure gradient force ( $\text{m s}^{-2}$ ) (b, d, and f) for  $dx = 128$  km (the first row) and  $dx = 8$  km (the second and third rows) at 4.5 km altitudes at 1400 UTC 20 May. (e) and (f) are the closer look of black box in (c) and (d), respectively.

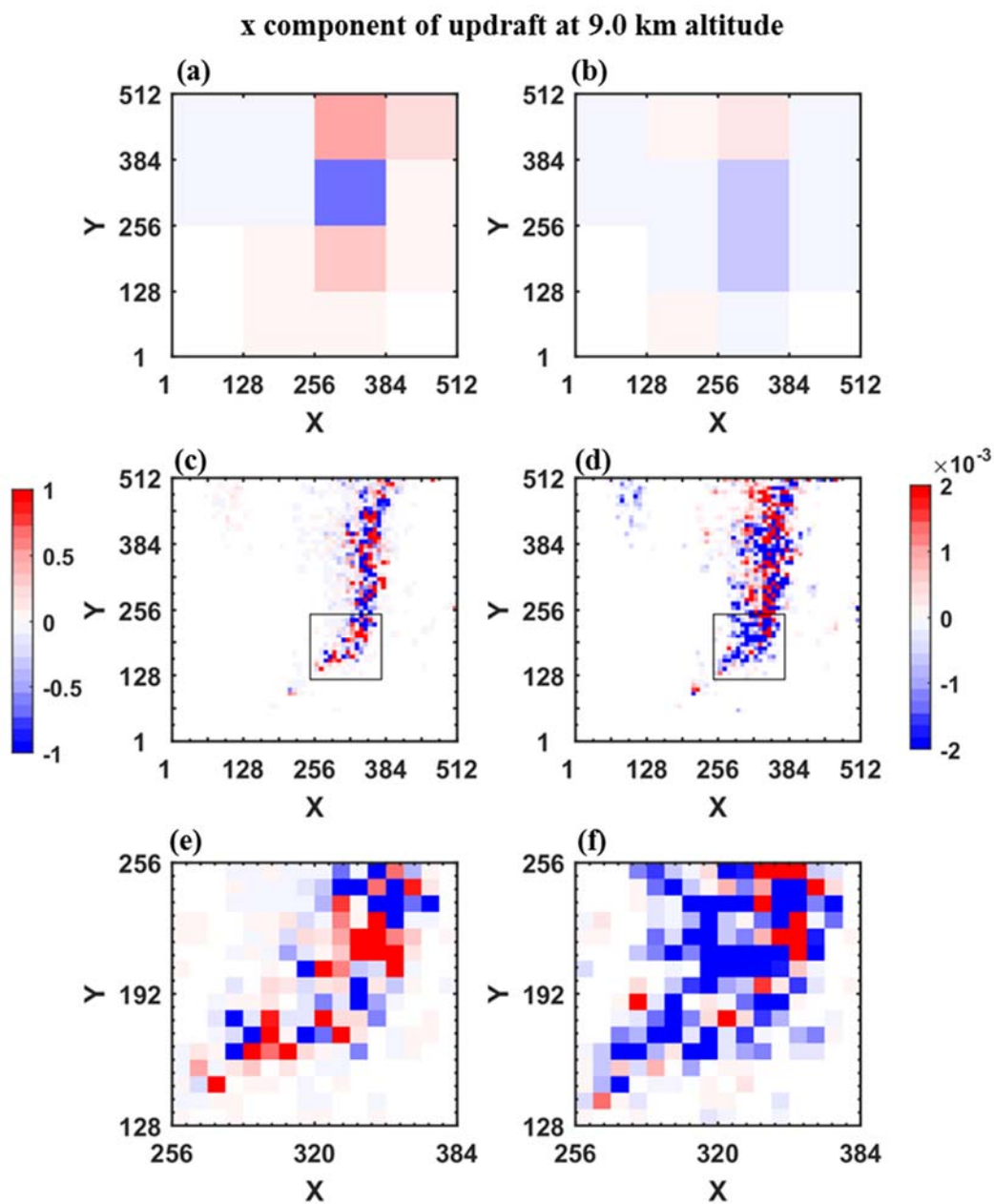
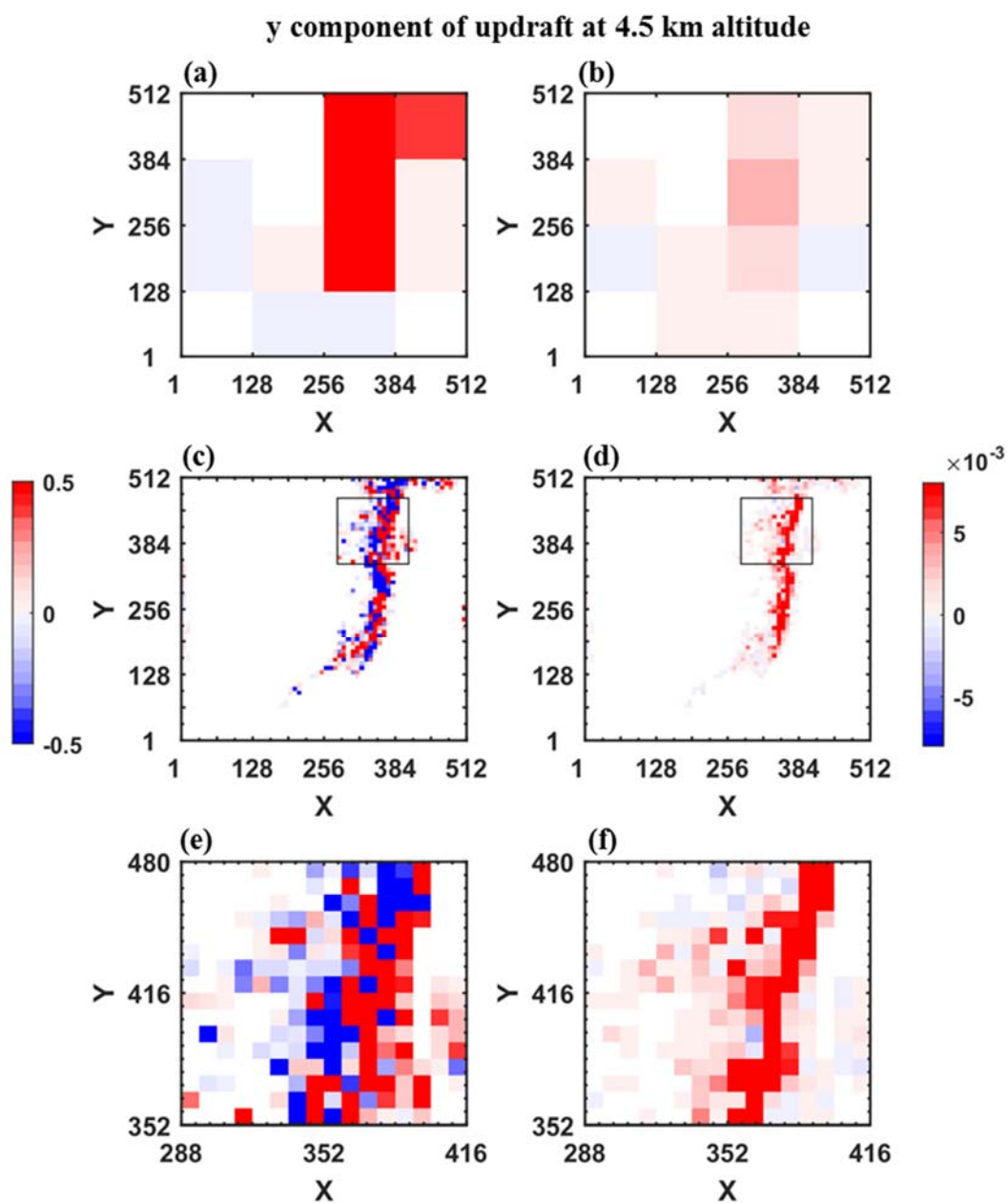


Figure 9. Same as Figure 8, except for x component at 9 km altitude.

995



996

997 Figure 10. Same as Figure 8, except for y component at 4.5 km altitude.

998

999

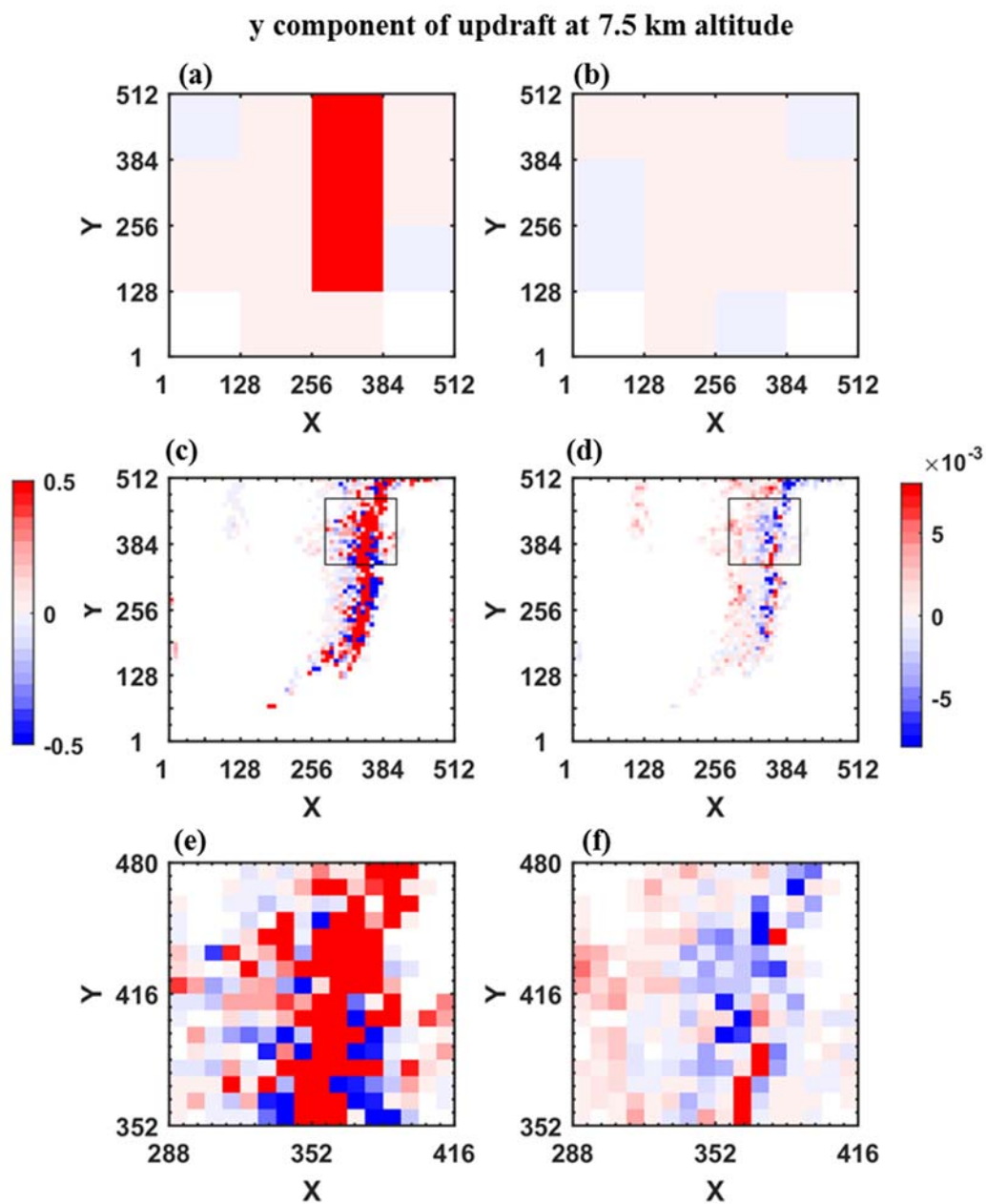


Figure 11. Same as Figure 8, except for y component at 7.5 km altitude.



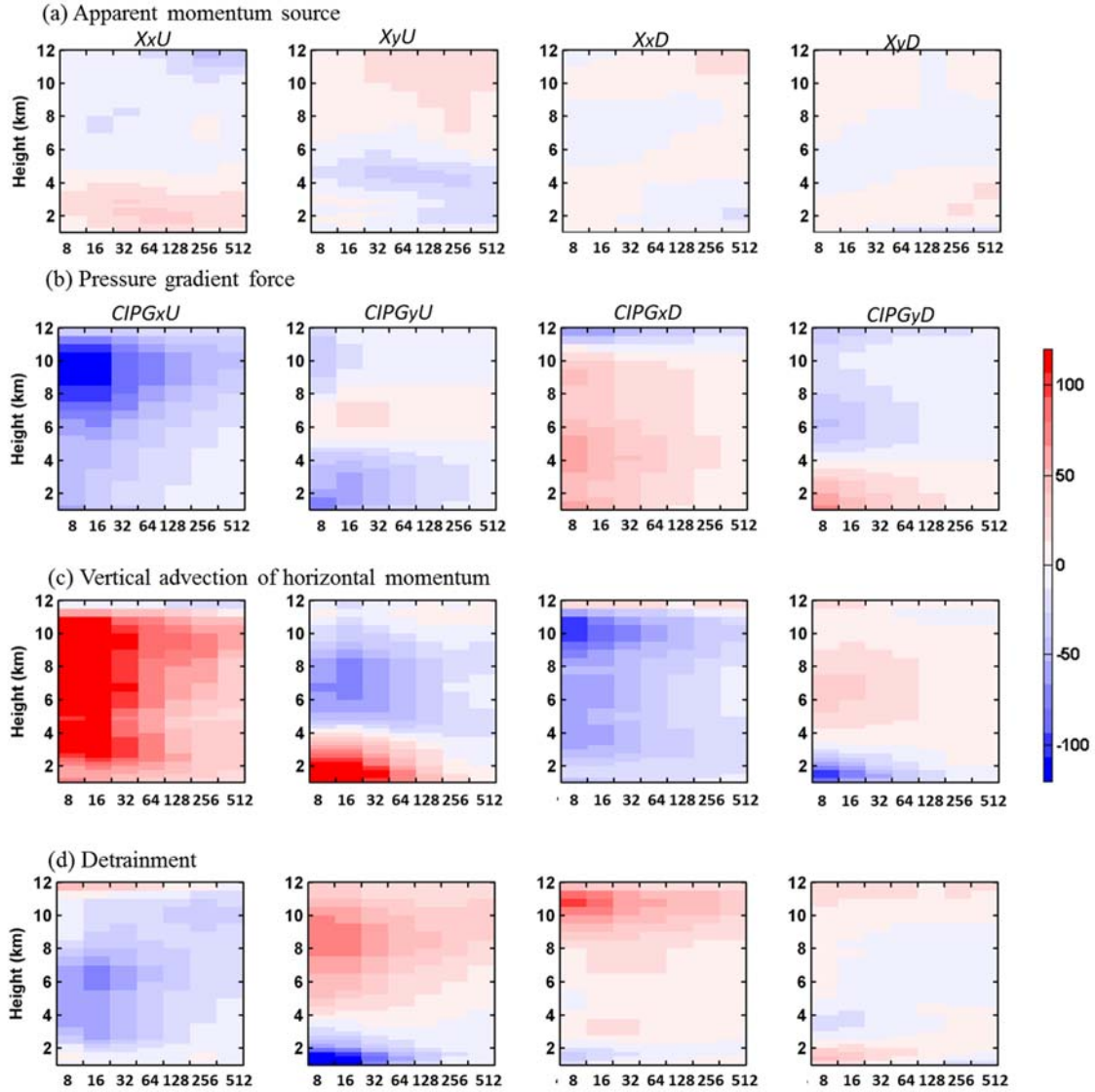


Figure 12. Vertical profiles of scale dependency of (a) apparent momentum source ( $\text{m s}^{-1} \text{ day}^{-1}$ ), (b) CIPG ( $\text{m s}^{-1} \text{ day}^{-1}$ ), (c) vertical advection by the compensating subsidence ( $\text{m s}^{-1} \text{ day}^{-1}$ ), and (d) horizontal momentum detrainment ( $\text{m s}^{-1} \text{ day}^{-1}$ ) for MC3E-0523. The panels from left to right are x component of updrafts, y component of updrafts, x component of downdrafts, and y component of downdrafts, respectively.



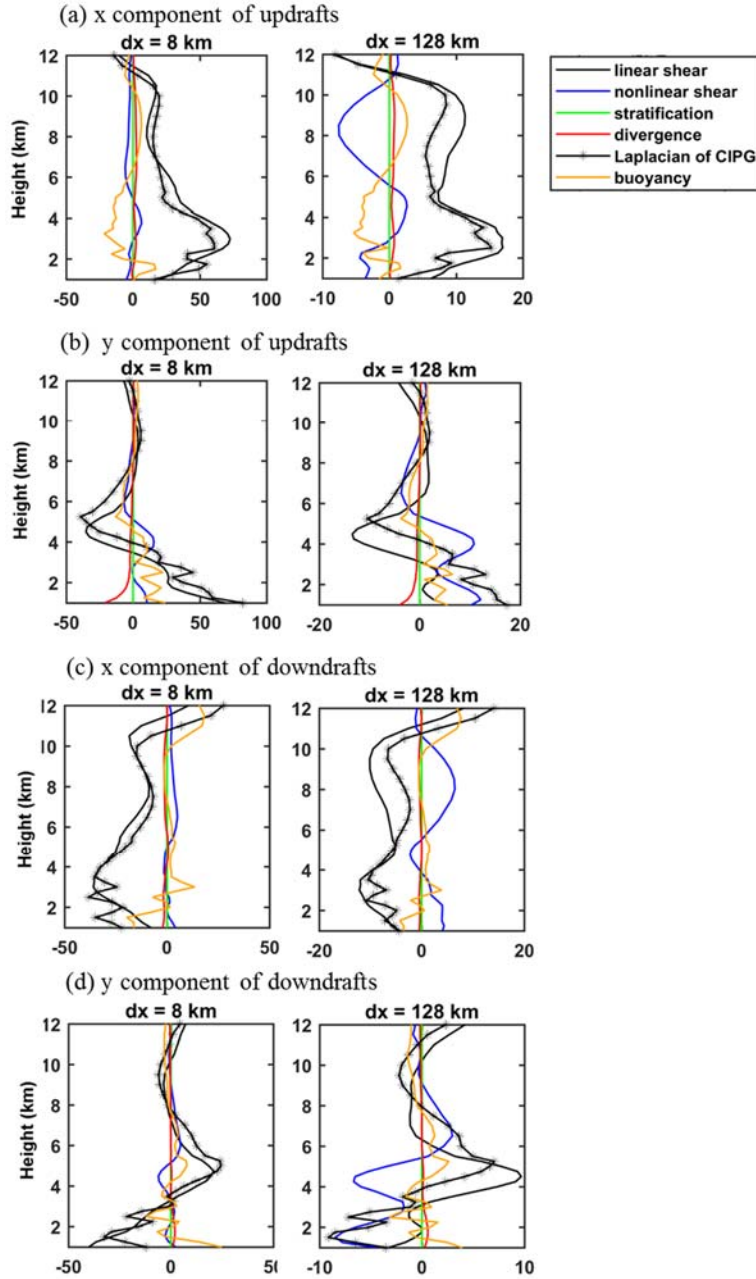


Figure 13. Linear-shear forcing (black line,  $10^{-11} \text{kg m}^{-4} \text{s}^{-2}$ ), nonlinear-shear forcing (blue line,  $10^{-11} \text{kg m}^{-4} \text{s}^{-2}$ ), stratification forcing (green line,  $10^{-11} \text{kg m}^{-4} \text{s}^{-2}$ ), divergence forcing (red line,  $10^{-11} \text{kg m}^{-4} \text{s}^{-2}$ ), buoyancy forcing (yellow line,  $10^{-11} \text{kg m}^{-4} \text{s}^{-2}$ ), and the Laplacian of CIPG (black line with asterisk markers) over (a) x component of updrafts, (b) y component of updrafts, (c) x component of downdrafts, and (d) y component of downdrafts for MC3E-0523. Please refer to Figs. S8 and S9 for the results of all different grid spacings.

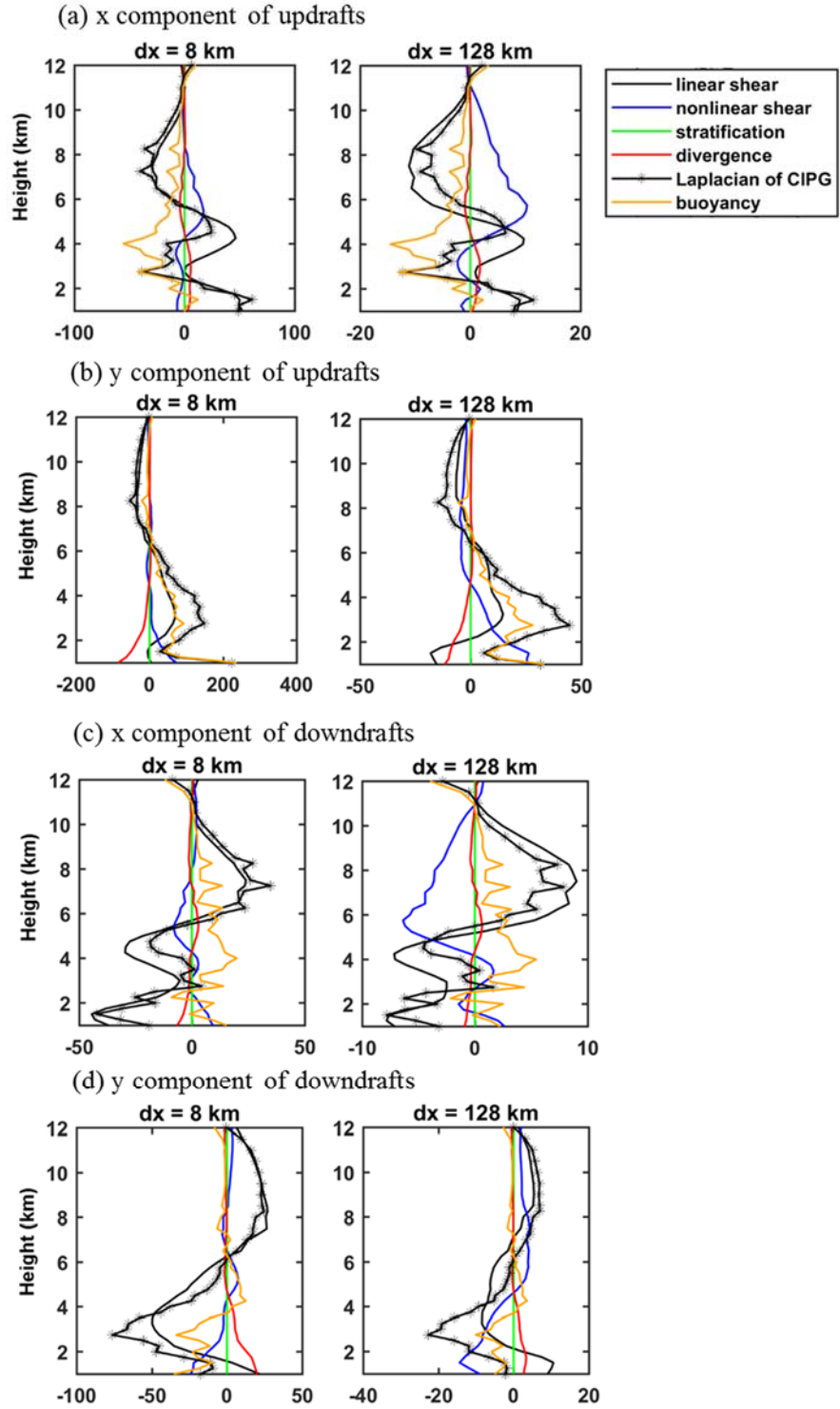


Figure 14. Same as Figure 13, except for MC3E-0520. Please refer to Figs. S10 and S11 for the results of all different grid spacings.

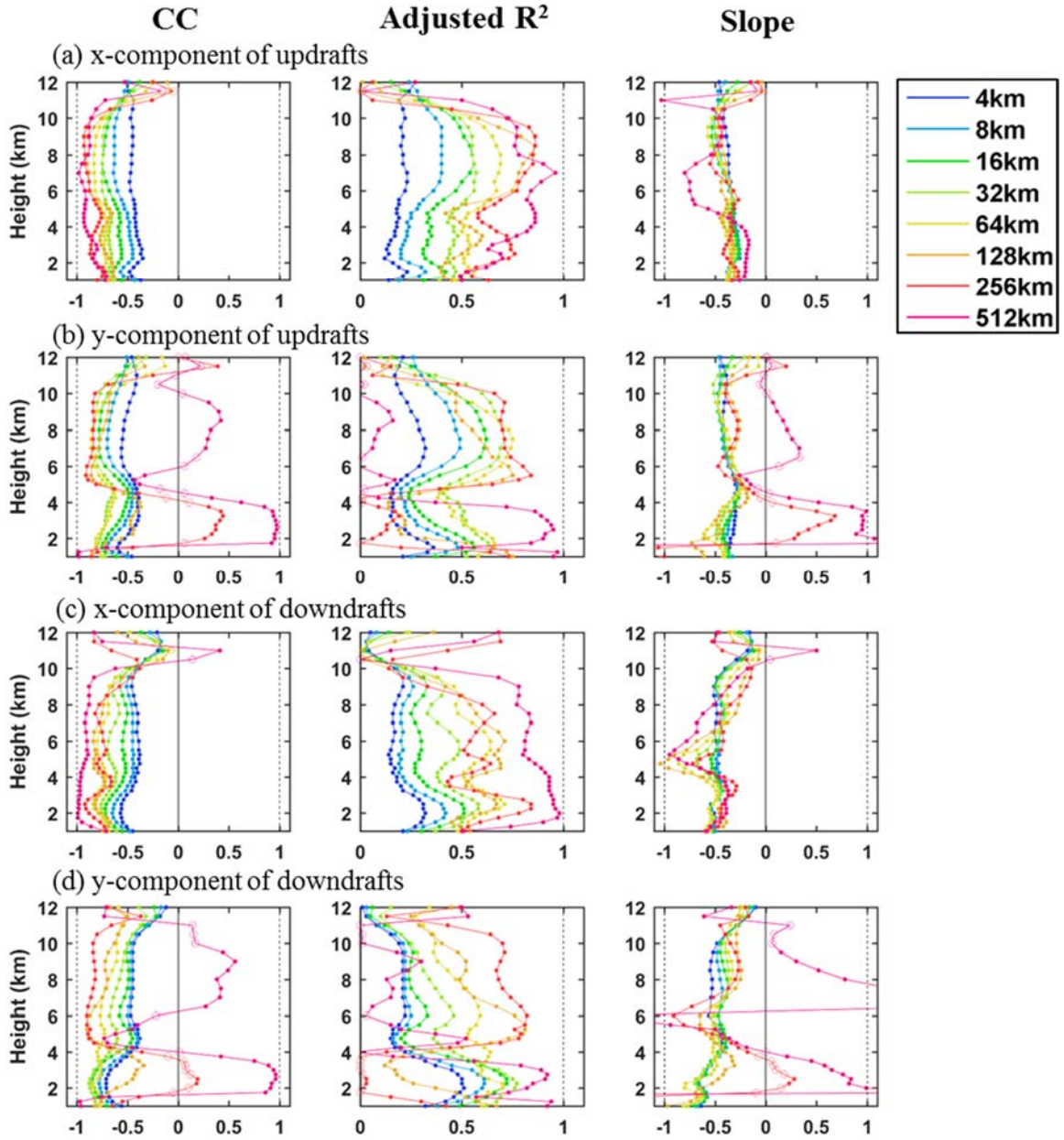


Figure 15. Vertical profiles of Pearson correlation coefficient (CC), adjusted coefficient of determination ( $R^2_{adj}$ ), and linear regression slope between CIPG and the product of mass flux and the vertical mean wind shear for (a) x component of updrafts, (b) y component of updrafts, (c) x component of downdrafts, and (d) y component of downdrafts from MC3E-0523. The hollow dots indicate where CC,  $R^2_{adj}$ , and linear regression slope are statistically insignificant.

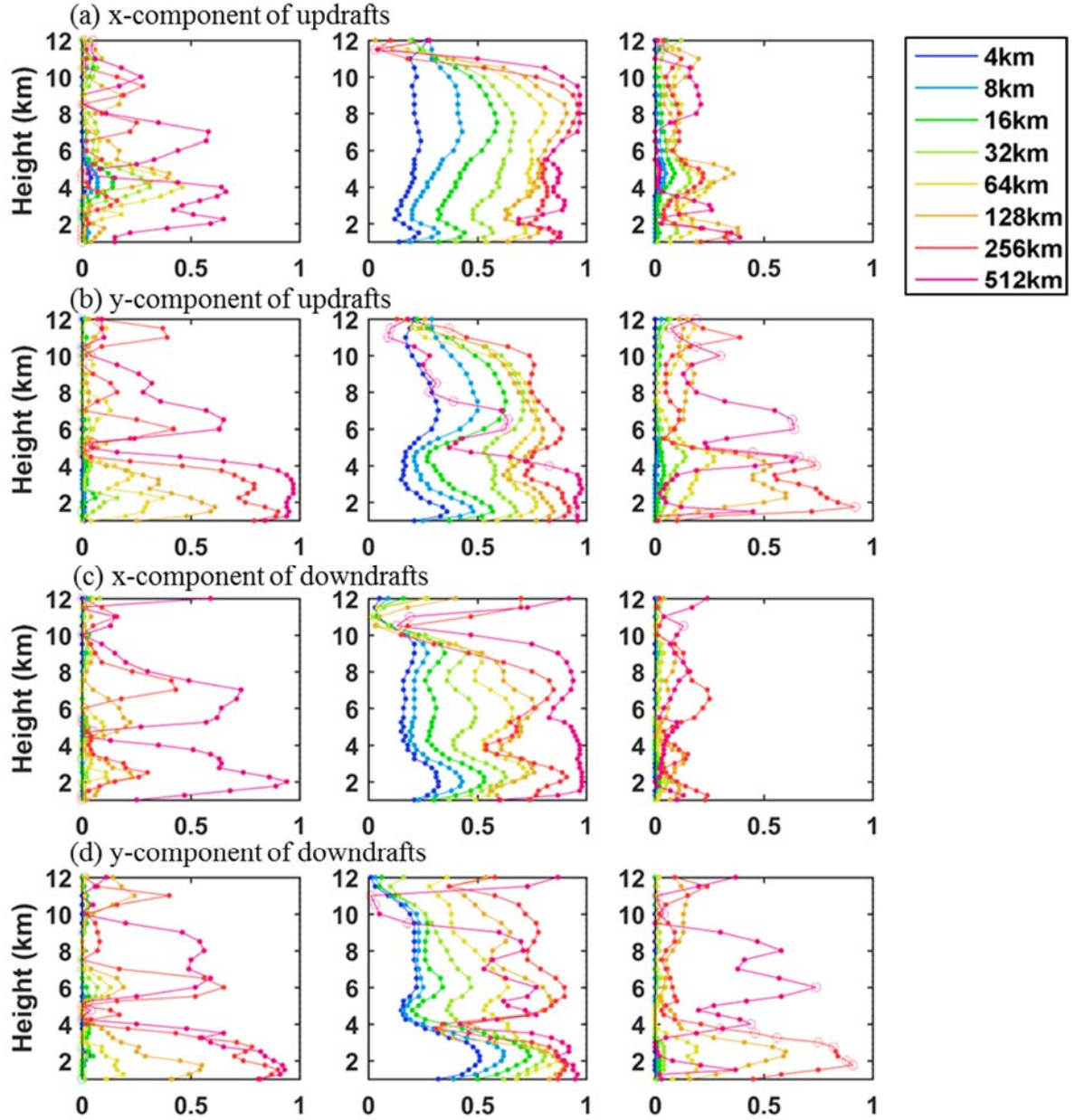


Figure 16. Vertical profiles of  $R^2_{adj}$  for product of mass flux and vertical perturbation wind shear (left column), the combination of product of mass flux and vertical mean wind shear as well as product of mass flux and vertical perturbation wind shear (middle column) as predictor variables with CIPG as response variable. The difference in  $R^2_{adj}$  between the middle columns in Figures 15 and 16 is also shown in the right column for (a) x component of updrafts, (b) y component of updrafts, (c) x component of downdrafts, and (d) y component of downdrafts from MC3E-0523. The hollow dots indicate where coefficients of determination are statistically insignificant.

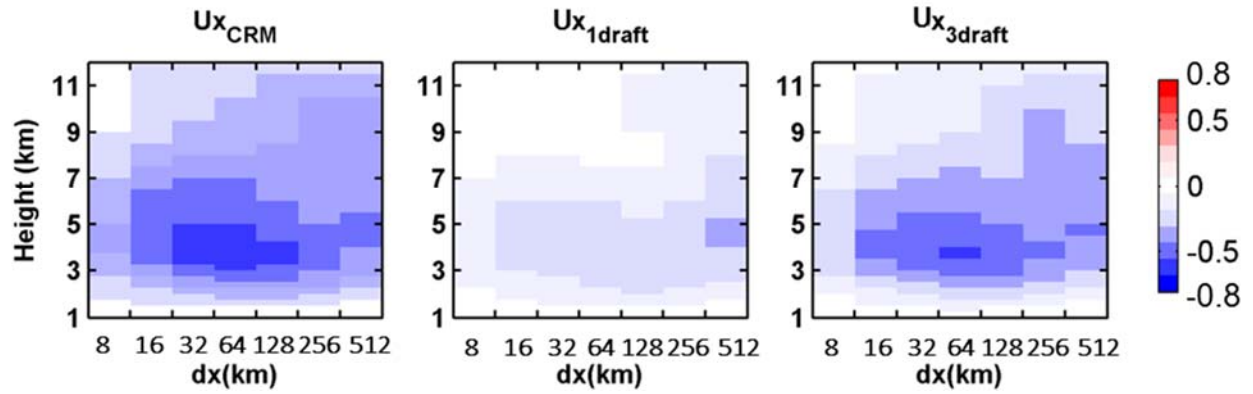


Figure 17. Vertical profiles of the scale dependency of the x component of updraft vertical momentum flux ( $\text{kg m}^{-1} \text{s}^{-2}$ ) from CRM, the one-updraft approach, and the three-updraft approach for MC3E-0523. Please refer to Figs. S14 and S15 for the results of x, y components of updraft, downdraft, environment and total vertical momentum fluxes.